FAKULTÄT PHYSIK
TECHNISCHE UNIVERSITÄT DORTMUND
LEHRSTUHL EXPERIMENTELLE PHYSIK Vb

Energy spectra unfolding of atmospheric neutrinos with the IceCube 22-string detector

Diploma thesis

by

Anne Wiedemann

Dortmund, October 2008

Contents

1

Introduction

Since its beginning astronomy has made fundamental contributions to our understanding of the universe. By means of optical telescopes new roads were traversed to uncover hidden areas of space and every new telescope technology was aligned to new discoveries and knowledge which have fundamentally stamped our physical understanding of the world. Today astronomy embraces a broad spectrum of detection methods from the measurement of cosmic radiowaves to the detection of high energy gamma-rays and neutrinos. Ambitious experiments have been launched to extend conventional astronomy beyond wavelengths of 10^{-14} cm, or GeV photon energy. Besides gamma-rays, protons (nuclei), neutrinos and gravitational waves will be explored as astronomical messenger particles probing the extreme universe. High energy photons have been used to paint a picture of the non-thermal universe, but a more complete image of the hot and dense regions of space can be obtained by studying astrophysical neutrinos.

Neutrinos are valuable messenger particles because they can reach us through the light years undeflected by interstellar magnetic fields and intervening matter, because they are neutral and only interact weakly. In the energy region above 100 TeV, neutrinos are most likely the only particles that reach us from the inner source of astrophysical objects while still pointing back to them.

For their detection huge detector volumes of the order of giga-tons have to be instrumented. The IceCube Neutrino Observatory directly located at the geographical South Pole is the largest neutrino detector of the world. It is capable of observing interactions of all neutrino species up to extremely high energies, including those from extragalactic sources, like active galactic nuclei (AGN), gamma ray bursts (GRB) and supernova remnants just to name a few.

Instead of searching for neutrinos from either a specific time or location in the sky, diffuse analyses are searching for extra-terrestrial neutrinos from unresolved sources, isotropically distributed throughout the universe.

Neutrino telescopes detect the so called Čerenkov radiation in highly transparent deep water or ice from secondary particles produced in the interactions of high energy neutrinos. There they take advantage of the large cross section of high energy neutrinos and the long range of the muons produced. The detection is made difficult by the fact that for every muon from a cosmic neutrino IceCube detects a million muons more produced by cosmic rays in the Earth's atmosphere. In order to filter them out the search is restricted to the northern hemisphere since neutrinos are the only known particles that can pass through the Earth unhindered.

Since the flux of atmospheric neutrinos from the interaction of cosmic ray protons with the Earth's atmosphere is the only flux confidently measurable so far it is used as a calibration device and it is looked for an excess of astrophysical neutrino events over the theoretically expected atmospheric spectrum. This could then be an indication of an extraterrestrial neutrino flux signal. And as Francis Halzen states: "While the number of events with energies of tens of TeV is relatively low, we establish that this is optimally the energy region where the atmospheric neutrino background is suppressed and an excess from these sources can be statistically established." [HKO08] From the appearance of an extraterrestrial neutrino flux eventually we hope to denote particle acceleration processes in astrophysical objects. Further we shall confirm or eliminate theoretical predictions.

The scope of this thesis is to reconstruct the energy spectrum of an atmospheric neutrino flux from measurings of the IceCube 22-string detector configuration of the year 2007. Since the acceptance and resolution of the detector is limited, an immediate reconstuction of the atmospheric energy spectrum from measurement is not advisable. Therefore for this analysis an unfolding method is used for reconstruction which was further successfully applied by [Mue07, Lue07] in connection with the Antarctic Muon And Neutrino Detector Array (AMANDA). A pure data sample of measured muon tracks stemming from atmospheric neutrinos is necessary to fulfill this task. In order to strongly reduce the dominant part of background events, two different approaches are studied in this thesis, namely a graphical cut on selected parameters as well as a classifier algorithm. The latter is for the first time applied for IceCube analysis.

2

Theoretical Fundamentals on Neutrino Astrophysics

2.1 Neutrinos and Cosmic Rays

A major reason for neutrino observation is to resolve the sources of high-energy cosmic rays. Cosmic rays were first observed in 1912 by Victor Hess who measured an increase of ionizing radiation with altitude in his famous balloon flight. Over the past decades numerous experiments have been conducted to measure the cosmic ray energy spectrum and its composition, from GeV energies up to 10^{11} GeV. The question of where and how in the universe cosmic rays are accelerated remains unanswered until today, mainly because the deflection of the charged particles in the magnetized interstellar medium washes out directional information.

The disadvantage of classical astronomies like observations in the radio, infrared, optical, ultraviolet, X-ray or γ-ray band stems from the fact that electromagnetic radiation is quickly absorbed in matter. With these astronomical methods one can solely observe the surfaces of astrophysical objects. In addition, energetic γ-rays from distant sources are attenuated via $\gamma\gamma$ interactions with photons of the black-body radiation by pair production. Charged primaries instead are deflected by interstellar magnetic fields and lose their directional information. The direction is only conserved for very energetic protons ($>10^{10}$ GeV) which in turn lose their energy via interactions with the cosmic microwave background (Greisen-Zatsepin-Kuzmin cutoff [Gre66], [ZK66]). Thus for protons with energies exceeding $6 \cdot 10^{10}$ GeV the universe is no longer transparent. As a consequence neutrinos are the only available carrier of information about cosmic ray origin over a long range fulfilling different requirements which makes them an ideal astronomical messenger particle. Being neutral, it is not influenced by magnetic fields, it does not decay, having a very low interaction probability it can penetrate from the central part of the source and is not absorbed by interstellar nor intergalactic dust nor by the infrared nor by black-body radiation. The detection of cosmic high energy neutrinos sources would be an unambiguous sign for hadron acceleration and interaction since they can only be produced by the decay of charged mesons.

In Figure 2.1 a schematic view of astrophysical particle propagation from an astrophysi-

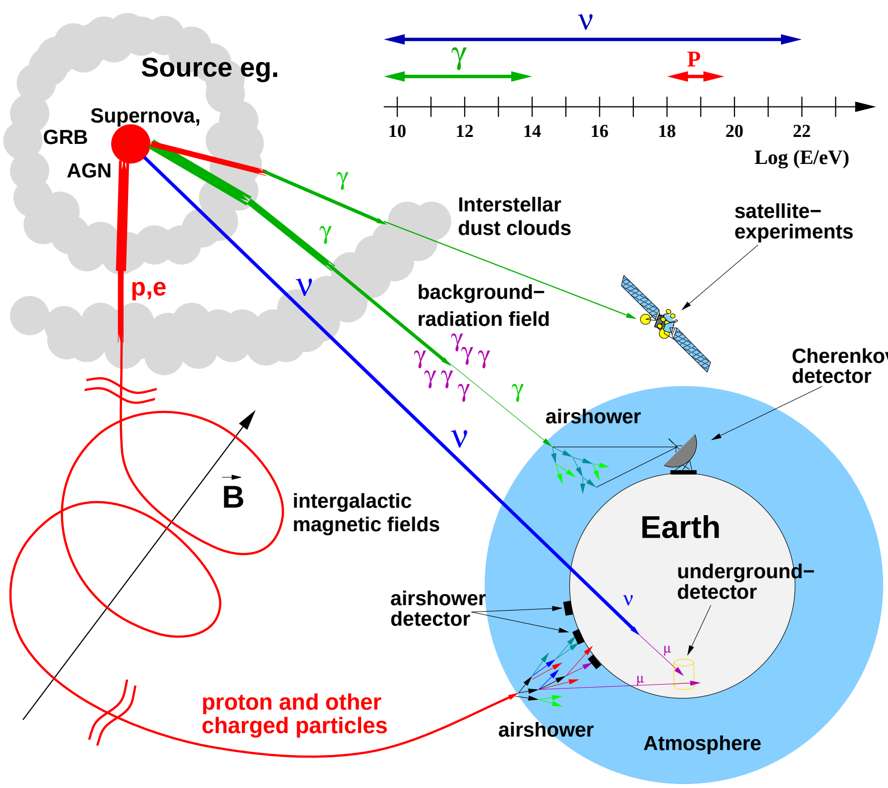

Figure 2.1: Schematic illustration of astrophysical particle propagation through the interstellar space and their detection on Earth. Top left: Energy scale of the particle emission. [Wag04]

cal source to the Earth is shown. On the right margin there is an energy scale of particle emission.

There are three different neutrino spectra that can be produced by comic rays. Atmospheric neutrinos, neutrinos produced by galactic cosmic rays in interactions with interstellar gas, and neutrinos generated by cosmic rays at their acceleration sites. Atmospheric neutrinos have been detected and intensively studied. Their production and flux characteristics are described in detail in section 2.3. The existence of neutrinos associated with cosmic ray sources has not yet been confirmed by observation. The requirements on acceleration processes as well as astrophysical objects considered to be sources of high energy neutrinos are illustrated in section 2.2.

2.1.1 Cosmic Rays

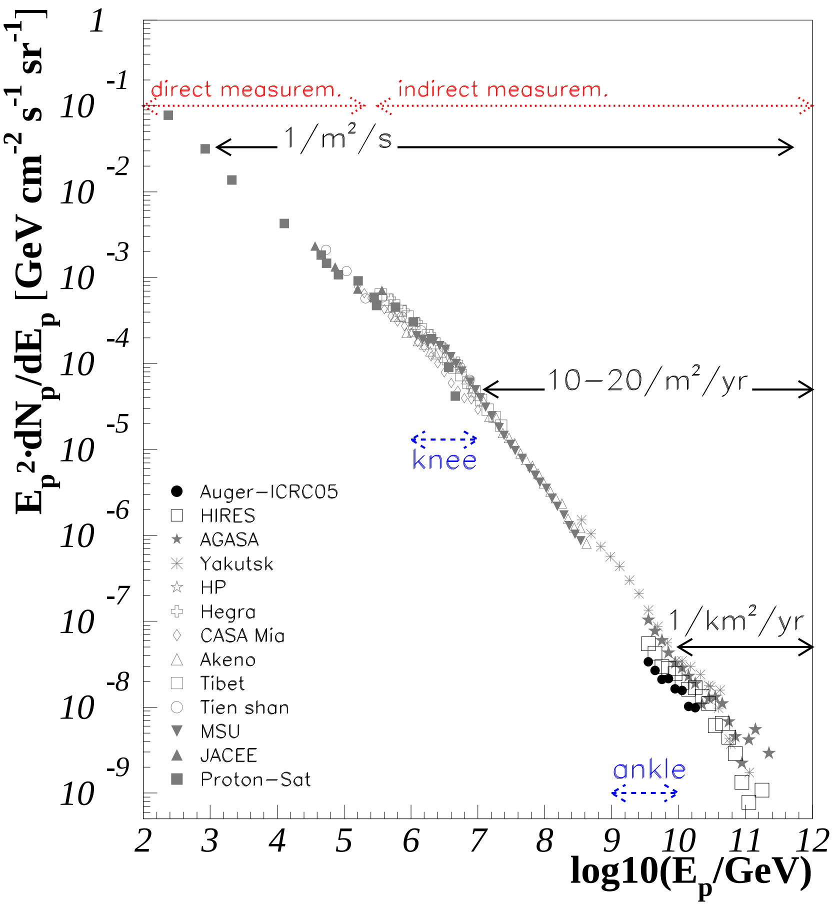

Figure 2.2: All particle cosmic ray spectrum. The data points are measurements from the experiments listed on the bottom left. [Som05]

Cosmic Rays are high energetic charged particles striking the Earth isotropically due to the deflected trajectories by magnetic fields in our galaxy and beyond. The main component of the primary cosmic ray flux are charged nuclei (98%) ranging from protons to the heaviest stable elements. Also electrons, anti-protons and gamma-rays have been identified. When cosmic rays are impinging the atmosphere, extended showers of secondary particles are generated through hadronic interactions of the primary protons with the atoms of the air or by decaying. The associated decay channels are as follows:

$$
\begin{aligned}
p + A &\rightarrow K^{\pm} + X && (2.1)\\
&\quad \hookrightarrow \mu^{\pm} + \nu_\mu(\bar{\nu}_\mu) && (2.2)\\
&\qquad \hookrightarrow e^{\pm} + \nu_e(\bar{\nu}_e) + \bar{\nu}_\mu(\nu_\mu) && (2.3)\\
p + A &\rightarrow \pi^{\pm} + X && (2.4)\\
&\quad \hookrightarrow \mu^{\pm} + \nu_\mu(\bar{\nu}_\mu) && (2.5)\\
&\qquad \hookrightarrow e^{\pm} + \nu_e(\bar{\nu}_e) + \bar{\nu}_\mu(\nu_\mu) && (2.6)
\end{aligned}
$$

Cosmic rays have been observed over many orders of magnitude from energies of GeV up to $3 \cdot 10^2$ EeV, an energy unit normally preserved for macroscopic objects. Fig. 2.2 shows the measured cosmic ray flux between 10^2 GeV and 10^{12} GeV. While there is still a large uncertainty in the normalization of the flux between the different experiments, the slopes of the energy spectra correspond well. Over many orders of magnitude the differential flux follows a power law of the form:

$$\Phi(E) \propto E^{-\delta}. \qquad (2.7)$$

In the high energy range, two characteristic features are visible: Above the knee, at $4 \cdot 10^6$ GeV, the spectral index steepens from $\delta = 2.7$ to $\delta = 3.1$. Above the ankle, at about 10^{10} GeV the spectrum flattens again to steeply drop at $5 \cdot 10^{10}$ GeV [Rf08]. There are explanations for the spectral power law behavior for the different energy ranges. Up to the knee it is believed that the cosmic rays are galactic in origin and are accelerated in shock waves resulting from supernova explosions. The knee results from the fact that galactic sources are not expected to be able to accelerate particles above a few PeV per nuclear charge Z. Even if it were so, above the ankle the gyroradius of a proton in the galactic magnetic field exceeds the size of the Galaxy and would escape.

The shape of the spectrum above the knee is then determined by the individual cut-offs in energy of the different elements, which is $\propto Z$. The possible existence of a second knee at $5 \cdot 10^8$ GeV supports this theory, since it could originate from the energy cut-off of the heaviest elements.

At the ankle extra-galactic cosmic ray emitters become dominant, which can accelerate particles to energies beyond 10^{11} GeV. The steep drop in the spectrum above $5 \cdot 10^{10}$ GeV is called the "Greisen-Zatsepin-Kuzmin cut-off" [Gre66], [ZK66]. It results from the interaction of high-energetic protons with the 2.7 K cosmic microwave background radiation by producing pions via the Δ-resonance. The decaying Δ emits a lower-energy proton. This energy loss process limits the range of the highest energetic protons to about 100 Mpc [Kf08].

Speaking of cosmic ray origin one has to distinguish between the power source and the acceleration site. Generally one assumes that in most cases cosmic-rays are not only generated in the source but also accelerated to high energies in or near the source. Possible sources for cosmic ray production and acceleration are supernova explosions, highly magnetized spinning neutron stars, i.e. pulsars, accreting black holes, and the centers of AGN's [Gru05]. On the other hand it is also possible that emitted cosmic-ray particles are further accelerated during their propagation in the interstellar or intergalactic medium by interactions with extensive gas clouds, which are produced by magnetic-field irregularities.

There exists a large number of cosmic ray acceleration models which explain different energy regions of the observed spectrum. The cyclotron mechanism and the acceleration mechanism by sunspot pairs in stars (see [Gru05] for details) are possibly responsible for the lower energy region up to GeV energies.

For the highest energy cosmic rays there exist two different models: the *top-down-* and *bottom-up-model*. In the as *top-down* classified model it is assumed that cosmic rays are the product of cosmological remnants or the decay of topological defects, domain walls or cosmic strings, which could be relicts of the big bang [Gru05].

The bottom-up model predicts cosmic accelerators as sources of high energetic cosmic rays and is given by the mechanism of stochastic acceleration at shock fronts. Supernova remnants are special means for cosmic ray acceleration because they have higher magnetic fields than the average interstellar medium. They are also large and have an adequate livetime to lead the acceleration process to higher energies.

2.1.2 Fermi Acceleration Mechanism

The idea of stochastic particle acceleration was first developed by E. Fermi. The main idea of the Fermi acceleration is that charged particles can gain energy in a large number of acceleration cycles by interacting with interstellar clouds. The observed power law spectrum can statistically be deduced from the following calculations.

Single acceleration cycle

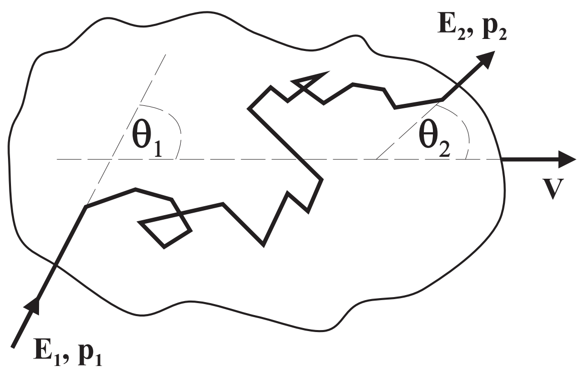

Figure 2.3: Second order Fermi acceleration. [Pro98]

Assuming a particle of Energy E_0 that encounters a massive cloud containing turbulent magnetic fields. In the lab system the particle and the cloud are moving towards each other. If the particle is relativistic then $E_0 \simeq p_0 c$. The cloud has infinitive mass and velocity v_{cl}. Assuming further for means of simplicity that the particle enters the cloud at an angle zero with respect to the direction of the cloud's velocity. Let the particle enter the cloud, scatter many times in the magnetic turbulence and come out of the cloud moving in a direction collinear and opposite to its initial direction, as shown in Fig. 2.3.
The particle energy in the cloud system is:

$$E_0^* = \gamma_{cl}(E_0 + \beta_{cl} p_0), \tag{2.8}$$

while $\beta_{cl} = v_{cl}/c$ and $\gamma_{cl} = \frac{1}{\sqrt{1-\beta^2}}$. Since the interaction of the particle with the magnetic cloud will be elastic, the particle energy and its momentum will not change. The energy E_1 of the particle leaving the cloud will be:

$$E_1 = \gamma_{cl}(E_0^* + \beta_{cl} p_0^*). \tag{2.9}$$

The relative energy gain ΔE of the particle follows as:

$$\frac{\Delta E}{E} = \frac{E_1 - E_0}{E_0} = \gamma_{cl}^2(1+\beta_{cl})^2 - 1. \tag{2.10}$$

It is proportional to the square of the velocity of the magnetic cloud. The energy gain depends strongly on the angles between the direction of the exit and entry of the cloud with respect to the cloud velocity vector. For the configuration that the particle leaves the cloud at its far side, keeping its initial direction, the energy gain would be zero. The particle may even lose energy when it enters the cloud along the cloud's velocity.

Let the particle now enter and leave the cloud with an angle different from zero. The transformations in equations (2.8) and (2.9) in this case include a term $\cos\Theta\beta_{cl}$ where Θ is the angle between the particle and the direction of the cloud's velocity. Since the particle's direction inside the cloud is fully isotropized through multiple scatterings, the exit angle is random and the average value $\langle\cos\Theta_2\rangle = 0$. The entry angle instead depends on the cloud's velocity and $\langle\cos\Theta_1\rangle = -\beta/3$. The average energy gain per cloud encounter then becomes:

$$\frac{\Delta E}{E} \simeq 4/3\beta_{cl}^2 \equiv \Xi. \tag{2.11}$$

After n encounters the particle energy will be:

$$E_n = E_0(1+\Xi)^n \tag{2.12}$$

and the number of encounters needed to reach the energy E_n is therefore:

$$n = \ln\left(\frac{E_n}{E_0}\right) / \ln(1+\Xi). \tag{2.13}$$

The particle can escape from the acceleration region with some probability P_{esc}. Thus the probability that the particle has remained in the acceleration region to encounter n magnetic clouds and has so reached the energy E_n is $(1-P_{esc})^n$.

Furthermore the number N of particles that reach energies higher than E_n is proportional to the number of particles that remain in the acceleration region for more than n encounters. With these considerations and using (2.13) it follows:

$$N(>E_n) = N_0 \sum_n^{\infty}(1-P_{esc})^m \propto A\left(\frac{E_n}{E_0}\right)^{-\gamma}, \tag{2.14}$$

with

$$\gamma \simeq P_{esc}/\Xi. \tag{2.15}$$

Stochastic acceleration thus generates power law energy spectra, and in the special case of Fermi acceleration the power law index depends on the square of β_{cl} as one also speaks of second-order Fermi acceleration.

Particle Acceleration at Shock Fronts

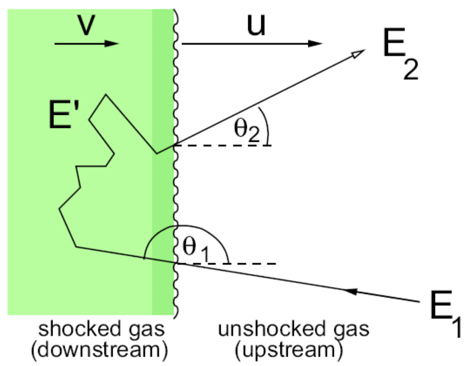

Figure 2.4: Schematic view of first order Fermi acceleration by a schock front in the interstellar medium. The "downstream" region corresponds to the schocked gas, the "upstream" region to the unschocked gas [Ack06a].

The shock front of an expanding supernova remnant is another possible location where stochastic acceleration may occur. The shock front is formed because the expansion velocity of the supernova remnant v_r is much higher than the velocity of sound in the interstellar medium. Therefore the shock runs ahead of the expanding remnant with velocity v_s. If the radial dimensions of the shock front are much larger than the gyroradius of the particle in the interstellar magnetic field, the shock can be regarded as a plane, as it is shown in Figure 2.4. Assuming the shock front moving with a velocity $u_1 = v_2$ and the gas behind the shock front receding with a velocity u_2 then the gas has a velocity $u_1 - u_2$ in the lab frame . Relativistic particles are crossing the shockfront and are moving in the downstream region, where they are either deflected out or scattered back and then they cross the shock again in the upstream region. During this scenario the particles always gain energy because the collisions are head-on in the corresponding frames. The acceleration process continues until the particles diffuse or are moved out of the shock region. Summing over all possible angles when entering or leaving the front, the energy gain per crossing becomes:

$$\Xi \sim 4/3\beta_s, \tag{2.16}$$

while β_s is the relative velocity of the shock front [Sta04].
Because the energy gain is proportional to β rather than β^2 the acceleration process is respectively called first-order Fermi acceleration. First-order Fermi acceleration is many orders of magnitude faster and more efficient than second-order Fermi acceleration. Particularly because the ejected envelope of the supernova has a much higher velocity than the average interstellar gas cloud.
The spectral index of strong shocks, with a shock velocity v_s much larger than the velocity of sound c_{sound} in the shocked gas, can be derived to be:

$$\gamma \approx -(2 + 4/M^2), \tag{2.17}$$

with $M \equiv |\mathbf{u}| / c_{sound}$ [Gai90]. Comparing the derivated spectral index $\gamma \approx -2.1$ with that of the measured cosmic ray spectrum, one has to take a steepening effect of $\Delta\gamma \approx -0.6$ into account. This is caused by a finite escape probability of cosmic ray particles from our galaxy. The probability increases with energy. The combination of the source spectrum with an energy dependent escape probability can finally explain the observed approximated power law of the form:

$$\frac{\mathrm{d}N}{\mathrm{d}E} \propto E^{\gamma}, \qquad \gamma \approx -2.7 \tag{2.18}$$

of cosmic rays ranging from 10 GeV to 1 PeV [Gai90].

2.2 Sources of Astrophysical Neutrinos

Two sources of low energy astrophysical neutrinos have been confirmed so far. A continuous flux of MeV neutrinos originating from the sun has been observed in several experiments [Ans94, HIK+90]. The only detection of MeV neutrinos from outside the solar system was a short burst of neutrinos in coincidence with the supernova explosion 1987A [HKK+87, BBB+87]. An overview of the neutrino spectrum expected from meV up to EeV is illustrated in Fig. 2.5.

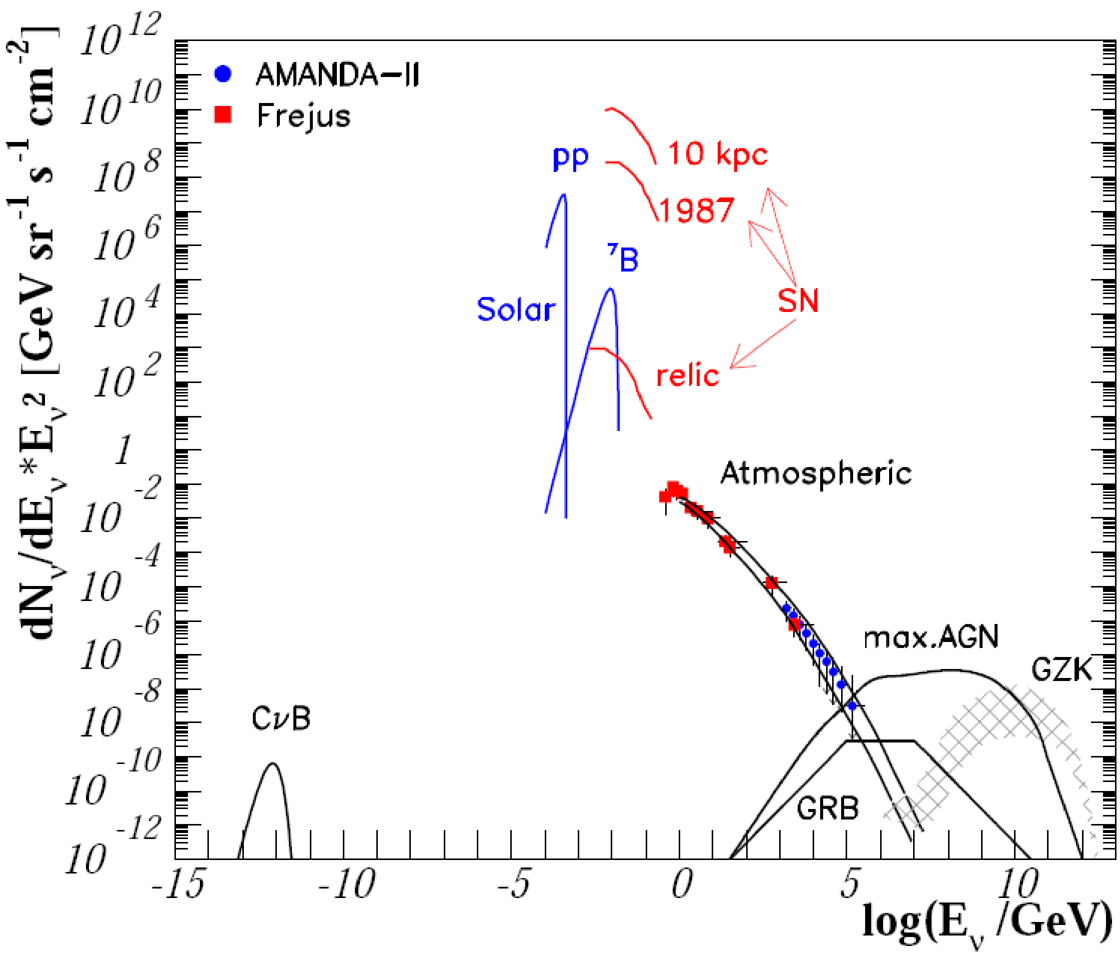

Figure 2.5: The astrophysical neutrino spectrum including different source predictions ranging from meV up to EeV. The fluxes of point sources have been scaled by $1/(4\pi)$ in order to be comparable to diffuse spectra. [Rou00]

High energetic astrophysical neutrinos are produced in shock fronts. The interaction of the ultra-relativistic particles with ambient low energy photons or protons leads to high energy γ-rays produced by inverse Compton scattering of electrons on photons. It can also lead to high energy pions produced in photo-meson interactions of protons and photons:

$$p + \gamma \rightarrow \Delta^+ \rightarrow p + \pi^0 \tag{2.19}$$

or

$$p + \gamma \rightarrow \Delta^+ \rightarrow n + \pi^+, \tag{2.20}$$

or in proton-proton interactions:

$$p + p \rightarrow \pi^0, \pi^\pm, \ldots \tag{2.21}$$

High energy γ-rays are then produced via $\pi^0 \rightarrow \gamma\gamma$ decays. High energy neutrinos are produced in the reactions $\pi^+ \rightarrow \mu^+ + \nu_\mu$, $\mu^+ \rightarrow e^+ + \nu_e + \bar{\nu}_\mu$ (or the charge conjugated reaction).

The sources of high energy neutrinos are assumed to be astrophysical objects which are known to emit high energy charged particles or $\gamma-$rays and are described in the following section.

Active Galactic Nuclei

Active Galactic Nuclei (AGN) are the most luminous objects observed in the universe so far. Besides they are the only extragalactic objects which have definitely been identified as sources of TeV $\gamma-$radiation. They are believed to be powered by a supermassive black hole in their center with a mass between $10^6 M_\odot$ and $10^{10} M_\odot$. A schematic view of an AGN is shown in Fig. 2.6.

The different observations of AGN differ by their various features in spectral shape, width of emission lines, and variability of the emitted γ-ray spectrum. The accreted matter from the black hole provides energy for the acceleration of electrons and possibly hadrons to relativistic velocities, causing the formation of two jets emitted along the nuclei's axis of symmetry. When these jets are pointed directly towards us, the AGN is classified as a blazar. If protons are accelerated in the AGN jets, we can also expect high-energy neutrinos to be produced in two different regions of the AGN. From the *core model* we can draw the assumption that the acceleration of protons happens in the accretion disc or in the jet close to the center. Interactions of high-energy protons with matter or thermal photons lead to neutral and charged pions and subsequently to the production of high-energy neutrinos and photons [Bec07].

From another model (*jet-model*), we derive that neutrino emission happens when protons, accelerated in the relativisticly moving jet, interact with ambient photons. Within the jet-model one has to distinguish two approaches for the high energetic γ-ray emission of blazars [Sta04]. On the one hand the pure leptonic channel approach assumes the photons stemming from synchrotron radiation of highly accelerated electrons in the jet. These relatively low energy synchrotron photons may further be pushed to higher energies by the inverse Compton effect. On the other hand from the pure hadronic approach of the jet-model we expect the gammas to be the decay products of neutral pions which on their turn are stemming from protons scattering off the surrounding matter. Especially this approach implies an expectation of a neutrino flux from the decay of the produced pions.

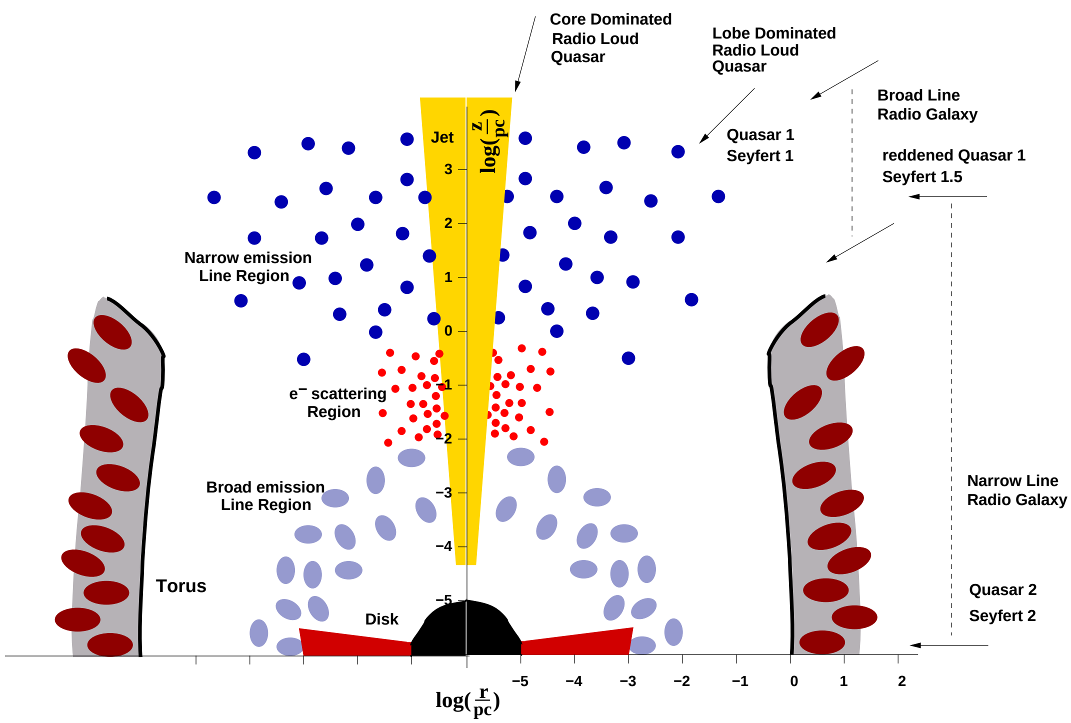

Figure 2.6: Scheme of a cylindrically symmetric AGN shown in the r-z-plane. Both axes are logarithmically scaled to 1 pc. [ZB02]

Gamma Ray Bursts

Gamma ray bursts are bursts of very high energetic photons over a short time scale of milliseconds to a few tens of seconds. In a GRB a solar mass equivalent of energy ($\sim 10^{53}$ erg) is converted into photons over a timescale of seconds with a very hard energy spectrum. From the leading model for GRBs we suggest that the high energetic photons are produced in a relativistic fireball expanding from the merger of two neutron stars or the collapse of a massive Wolf-Rayet-Star in a supernova explosion. In this explosion a jet is emitted along the axis of rotation of the system. Again protons might be accelerated in these jets by Fermi acceleration leading to neutrinos by pion-production and decay with energies of about 100 TeV [Wax00].

Microquasars

Microquasars are X-ray emitting binary star systems which eject relativistic jets perpendicularly to both sides of an accretion disc. The jets contain relativistic electrons that produce synchrotron radiation observed as radio wavelengths.
Microquasars more or less behave like extragalactic quasars. But their black hole has a mass density of a factor of a million solar masses less. One expects a neutrino flux from photon-meson production from proton and electron acceleration in the jets.

Supernova Remnants

A supernova can occur when a star gradually burns its hydrogen to helium then to carbon etc. The burning of the heavier elements begins in the center and proceeds in shells to the outer regions of the star. Finally a core of iron is built. Before this stage, an equilibrium of radiation and gravitational pressure is sustained. Once an iron core is created, no more energy can be released in nuclear fusion in the central region, and the star cannot longer withstand the gravitational force and as a consequence will collapse under its own gravity. So matter will be contracted in the center to a density comparable to the density in atomic nuclei.
The collapse leads to a shock wave ejecting the outer shell of the star at velocities of about 10^4 km/s, while a neutron star is formed at the center. Most of the energy released in the

collapse is emitted as neutrinos of energy of $\approx 10\,\mathrm{MeV}$ [BWC96]. Acceleration at the shock front, as described above, can create high energy particles which are believed to contribute significantly to the observed cosmic ray spectrum up to the knee described in section 2.1.1 ($\approx 10^6\,\mathrm{GeV}$) [LM00].

Pulsars

Pulsars are rapidly rotating neutron stars, which are remnants of supernova explosions [BWC96]. In this process neutrons are formed via weak interactions in the highly densed matter. The generated neutrons cannot decay via the beta decay into electrons because the Fermi energy of electrons in such a neutron star receives several hundred MeV. However the maximum energy which can be achieved by the electrons by the decay is only $0.78\,\mathrm{MeV}$, and thus all energy levels up to this energy and beyond are occupied, so that the Pauli principle is forbidding this process. [Gru05]. Pulsars are believed to have a co-rotating magnetic field of $\gtrsim 10^8$ T which creates strong electric fields. These fields can accelerate charged particles to the order of 10^{11} GeV. In this scenario neutrinos can be produced due to the interaction of relativistic hadrons with the pulsar's environment.

2.3 Atmospheric Neutrinos

In the case of atmospheric neutrinos one has to distinguish between conventional and prompt neutrinos, named after the decay channel involved in their generation. First considering conventional atmospheric neutrinos. These are predominantly produced in the Earth's atmosphere by the decay of charged pions via:

$$\pi^+ \quad \rightarrow \quad \mu^+ + \nu_\mu \tag{2.22}$$

$$\hookrightarrow e^+ + \nu_e + \bar{\nu}_\mu \tag{2.23}$$

$$\pi^- \quad \rightarrow \mu^- + \bar{\nu}_\mu \tag{2.24}$$

$$\hookrightarrow e^- + \bar{\nu}_e + \nu_\mu \tag{2.25}$$

$$\tag{2.26}$$

The contribution of kaons grows with energy. The decay length of a 1 GeV muon is about 6 km. Thus practically all muons decay before they interact. Therefore the resulting energy spectrum of atmospheric neutrinos follows the incident cosmic ray spectrum with $\gamma \sim 2.7$ up to $\sim 100\,\mathrm{GeV}$ and steepens towards $\gamma \sim 3.7$ at higher energies [GHS95]. It is about one power steeper than the primary spectrum, $\sim E^{-2.7}$, since a considerable fraction of pions and kaons ($\tau \sim 10^{-8}\,\mathrm{s}$) interact again before decaying. This process decreases with growing energy. The spectrum of conventional atmospheric neutrinos in the parametrization of [Vol80] is shown in Fig. 2.7. The dotted line represents the integrated neutrino flux over all zenith angles. There is an angular dependence of the neutrino spectrum intensity which increases at the horizon. This effect occurs because pions and muons that are produced nearly tangent to the Earth have more time to propagate in the less dense atmospheric region and thus have a higher decay possibility as opposed to vertical events.

So far we have only considered neutrinos stemming from the decay of pions, kaons and muons usually referred to as *conventional atmospheric neutrinos*. The (semi)-leptonic decay of charmed particles, produced by interactions of cosmic rays in the atmosphere, is also a source of atmospheric neutrinos - the *prompt atmospheric neutrinos*. Charmed particles have a short livetime and always decay before they interact in the atmosphere.

Thus, the prompt neutrinos continue with the same power as the primary spectrum to much higher energies, whereas the spectrum of conventional neutrinos becomes one power steeper for $E \gtrsim 1\,\mathrm{TeV}$. Prompt neutrinos may dominate the atmospheric spectra at energies above 10-100 TeV as a result of their flatter energy spectrum. For this reason, an estimate of prompt neutrinos is important for estimating the background for astrophysical neutrinos. The flux of prompt neutrinos is very difficult to predict theoretically because charm is produced by fusion of gluons at high energies. The low-x behavior of the gluon's structure function contributes to the cross section. In many models the theory of pertubative QCD

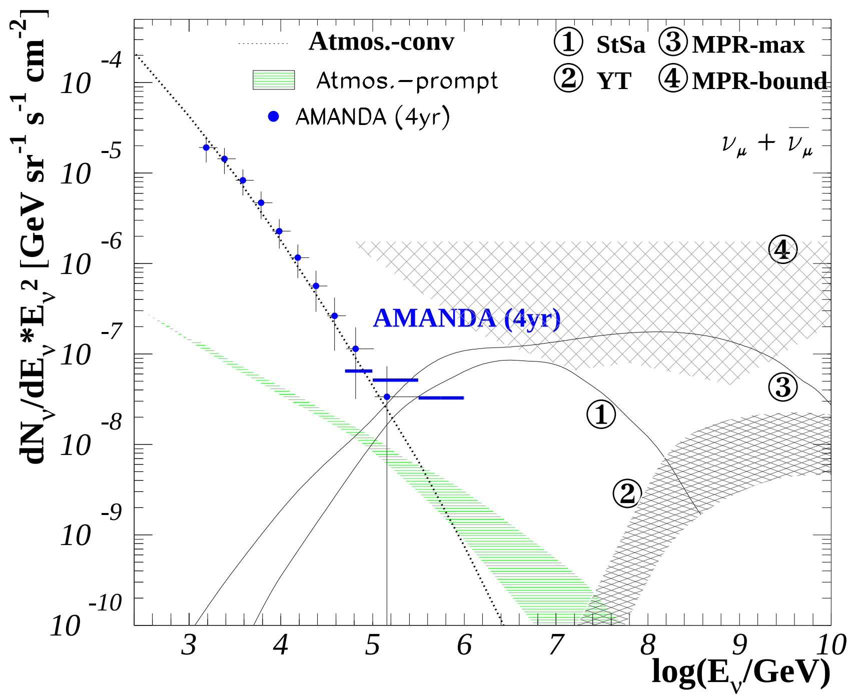

Figure 2.7: Muon neutrino flux predictions. (1) Neutrino flux expected from MeV-photon emitting blazars [SS96]. (2) Neutrino flux accounting for the absorption of protons by the GKZ effect [YT93]. (3) Neutrino flux representing the maximum contribution from TeV blazars [MPR01]. (4) An upper bound for optically thin (lower line) and optically thick (upper line) sources. Dashed line: The atmospheric neutrino flux after predictions from [Vol80]. Blue dots: Measurements for the atmospheric flux from AMANDA of the year 2000 [Mue07]. Blue vertical lines: Limits on the expected extraterrestrial neutrino flux from an AMANDA 4-year data analysis [Mue07]. Illustration from [Bec07].

is used to calculate the flux of prompt atmospheric neutrinos and the different models can vary in many orders of magnitude. Fig. 2.8 shows the contribution of the conventional and prompt atmospheric neutrino flux prediction as well as the resulting total flux for muons electron neutrinos and muon neutrinos. The flux is weighted with a factor E^3.

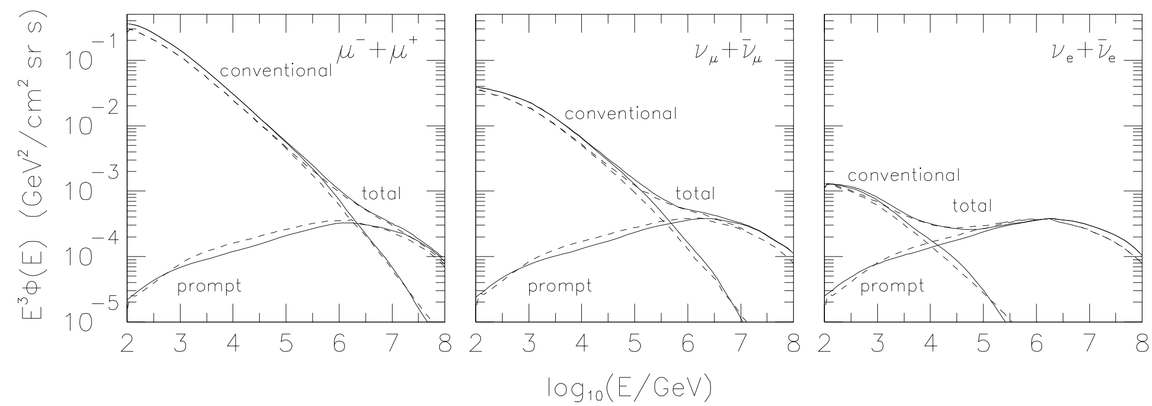

Figure 2.8: Vertical flux of muons, muon-neutrinos and electron-neutrinos weighted with E^3. The conventional and prompt flux components as well as the total flux are illustrated. The dotted and continuous line shows the results of the simulation for two different approximations [TIG96].

3

The IceCube Detector

IceCube is a Čherenkov detector with a volume of 1 cubic-kilometer being constructed below the surface at the geographical South Pole. Finally completed in 2010 it will consist of 4800 digital optical modules (DOMs) installed on 80 strings deployed in the ice bewteen 1450 and 2450 meters depth. In the horizontal plane the strings are arranged in a triangular pattern so that the distances between each string and its six nearest neighbors are 125 m. The detector is complemented by an air shower array, named IceTop. This is installed on the surface and will consist of 160 ice-tanks, in pairs, near the top of each IceCube string. Fig. 3.1 shows a schematical illustration of the detector configuration of the year 2007. The detector's predecessor AMANDA is also displayed as a part of the IceCube detector. AMANDA still serves for the study of low energetic neutrino events. The in ice detector is optimized for the detection of TeV muon neutrinos originating from cosmic ray sources. IceTop assists IceCube in the directional calibration and background rejection. In this chapter the physical principles of the detection of muon neutrinos are described, as well as the design and the data acquisition system of the IceCube detector.

3.1 Detection Principle

The IceCube neutrino detector does not directly observe neutrinos but it can detect secondary particles from the rare interactions of neutrinos with atoms of the atmosphere or rock of the Earth.

Even though the detector is optimized for the detection of muon neutrinos it has some sensitivity to other flavors. In the case of muon neutrinos we are looking for Čerenkov light emitted by relativistic muons (see section 3.1.1).

To detect these muons an instrumented volume of some clear material equipped with optical sensors is necessary. This has to be very large because of the very low cross sections of neutrino interactions.

The deep antarctic ice is especially suitable for this detection principle because it has particular optical properties. The absorption length for light from UV to blue varies between 50 and 150 m, depending on depth, which means that it can be seen quite far away from its source. On the other hand the scattering length averages about 20 m. This is on the same scale as the separation of the DOMs, which means that the light that is oberved by the optical modules is heavily scattered.

Dust layers originating from varying geological conditions over the millenia lead to a depth

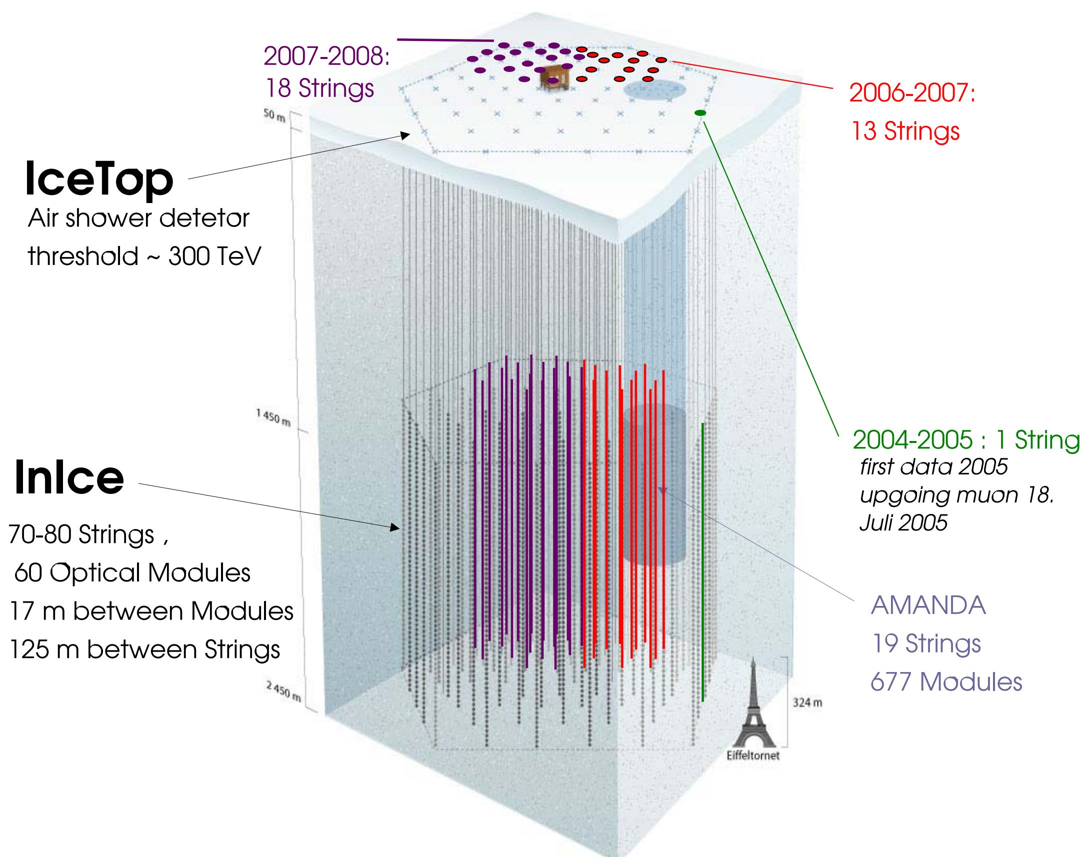

Figure 3.1: Schematical illustration of the IceCube 22-string detector. [The05]

dependence of the optical properties and may have dramatic effects on the measured data, which have to be taken into account during simulation and reconstruction.

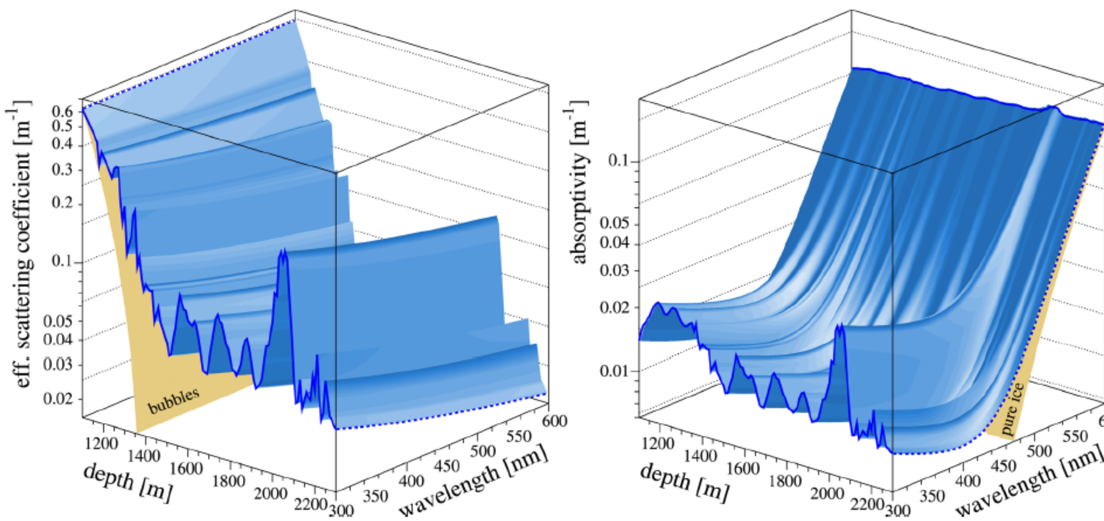

Figure 3.2: Illustration of optical scattering and absorption for deep South Pole ice. The depth dependence between 1100 and 2300 m and the wavelength dependence between 300 and 600 nm for the effective scattering coefficient (left) as well as for the absorptivity (right) are shown as shaded surfaces. Superimposed are the contribution of bubbles to the scattering coefficient and pure ice to the absorptivity as sloping surfaces (ochre). The dashed lines at 2300 m show the wavelength dependencies. of scattering and absorption. [Ack06b]

Figure 3.2 illustrates the absorptivity (right) and optical scattering for varying depth of the South Pole ice. Several peaks are visible as well as a particulary strong peak at a depth of 2000 m where the scattering length drops as low as 4 meters.

In order to succesfully detect muon neutrinos there has to be a strategy to separate them from the overwhelming background of muons produced by cosmic ray air showers. The strategy is twofold. Firstly, the detector is build far below the surface to help attenuate the cosmic ray muons. Secondly, we are looking for muons travelling upward through the detector using the Earth as a filter.

When an upgoing event is seen in the detector this must be a muon from a neutrino interaction; a comsic ray muon could not have penetrated more than a few kilometers through the Earth.

The cross sections for neutrino interactions are very small, varying between 10^{-10} and 10^{-7} mb in the energy range of interest. This makes neutrino astronomy a technical challenge.

Detecting a neutrino is possible if it undergoes a charged current or neutral current interaction with a nucleus within or close to the detector. In a charged interaction a lepton of the same flavor as the original neutrino is generated. While electrons lose their energy rapidly and taus decay very close to their production vertex, muons can travel long distances through the medium before decaying. So even muons generated far outside the detector, can be detected and the effective interaction volume for muon neutrinos is much larger than for the other flavors.

The calculated deviation angle between the track of the neutrino and the track of its secondary particle is less than one degree at 1 TeV and decreases at higher energies. For a given zenith angle, a neutrino must penetrate a certain amount of material to reach the detector volume. From the calculated cross section at a given energy one can determine the absorption lenght of the neutrino of that energy. Figure 3.2 left shows the absorption lengths of neutrinos traversing the Earth having energies ranging from 10 TeV to 10 PeV for different zenith angles.

According to this plot, very high energy neutrinos have an absorption lenght much larger than the Earth's diameter at high zenith angles. To detect these neutrinos the observation is restricted to the horizon.

The capabilities of a neutrino detector to measure cosmic neutrino fluxes can be quantified by two parameters, i.e. the effective area and the sensitivity.

The effective area can be seen as the aperture of an ideal neutrino telescope. The sensitivity otherwise is defined as the ability of the neutrino detector to exclude a certain flux intensity from the observed signal.

The neutrino effective area A^{ν}_{eff} relates the detectable neutrino event rate R_{ν} to the incident neutrino flux Φ. The parametrizations of the effective area allow to calculate event rates expected from a certain neutrino flux prediction and to make them comparable in different analysis techniques or experiments.

3.1.1 Energy Loss of Muons in Ice

A muon travelling through matter loses energy by ionization of the surrounding medium or by stochastic processes like bremsstrahlung, e^+/e^- pair production and photo-nuclear interactions.

The energy loss due to ionization proceeds continuously according to the Bethe-Bloch formula and can be approximated at a rate of

$$dE/dx \approx -2.6\mathrm{MeV}/(\mathrm{cm}^{-2})$$

for energies $E \gtrsim 10\,\mathrm{GeV}$.

The stochastic energy losses are dominant above an energy of $\approx 500\,\mathrm{GeV}$ resulting in a total average energy loss of

$$\frac{dE}{dX} = -a - bE, \tag{3.1}$$

with $a \approx 2.6\,\mathrm{MeV}/(\mathrm{g\ cm}^{-2})$ and $b \approx 4 \cdot 10^{-6}\ /(\mathrm{g\ cm}^{-2})$ for the energy loss in ice.

Solving this equation one finds a range R for muons of initial energy E_μ:

$$R = \frac{1}{b} \ln \left(1 + \frac{b}{a} E_\mu\right). \tag{3.2}$$

Thus, the average muon range varies between $\approx 350\,\mathrm{m}$ w.e. (water equivalent) for $E_\mu = 100\,\mathrm{GeV}$ and $\approx 31\,\mathrm{km}$ w.e. for $E_\mu = 10^9\,\mathrm{GeV}$. Figure ?? illustrates the survival probability of a muon at a certain distance, indicating the range calculated by 3.1.1.

Čerenkov light emission

Charged particles travelling through a medium with a velocity greater than the speed of light in this medium emit electromagnetic radiation. The moving particle polarizes the surrounding atoms or molecules, which quickly fall back to their ground states emitting radiation after the particle has passed. The light emission is illustrated in Figure 3.3. For a particle travelling faster than the speed of light in that medium, c_v/n, the light forms a coherent waveform propagating with an angle Θ_c to the incident particle trajectory. The angle is given as:

$$\cos\Theta_c = \frac{1}{\beta n}, \tag{3.3}$$

with $\beta = v/c_v$ and n the index of refraction in this medium. The particle energy for which $\beta n = 1$ and $\Theta_c = 0$ is called the Čerenkov threshold. For muons passing through ice the threshold is approximately 160 MeV. In the energy range of interest ($E \gg 10\,\text{GeV}$) one can safely both assume, $\beta = 1$ and therefore a Cherenkov angle of $\Theta_c \approx 41°$.
The spectral distribution of the emitted photons is given by the Frank-Tamm-Formula:

$$\frac{dN}{dxd\lambda} = \frac{2\phi\alpha}{\lambda^2}\left(1 - \frac{1}{\beta^2 n(\lambda)^2}\right), \tag{3.4}$$

where $\alpha \approx 1/137$ is the fine structure constant. For a constant index of refraction the number of photons emitted per unit length is inversely proportional to their wavelength and therefore the Čerenkov spectrum is peaked in the ultraviolet region. The energy loss due to this radiation is negligible compared to the other much dominant energy loss processes of the muon in ice [Ack06a].

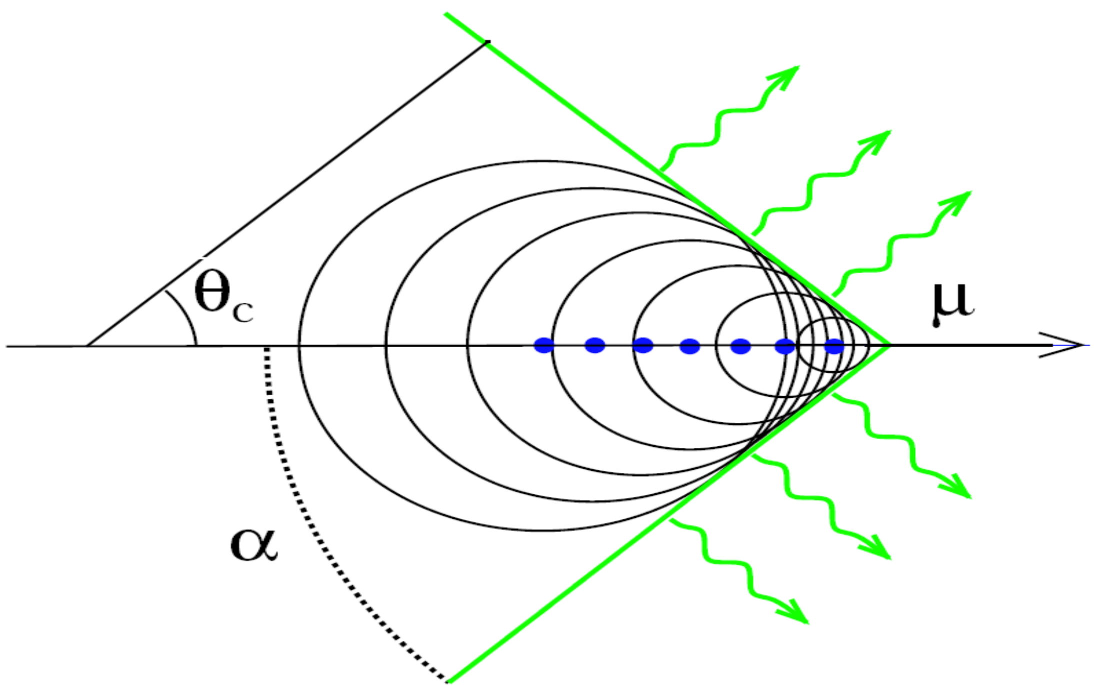

Figure 3.3: Two dimensional projection of a Čerenkov cone emitted along the particle trajectory. Θ_c denotes the angle between the particle trajectory and the propagation direction of the light [Ack06a].

3.2 Data Aquisition and Performance

The Digital Optical Module (DOM) is the most important part of the IceCube detector. A DOM is a piece of hardware that consists of a photo-multiplier tube (PMT) encased in a pressure sphere. Included in the DOM main electronic board are components to acquire, digitize and transmit digital signals to the surface, as well as components to assist in the calibration of the detector.

Two analog transient waveform digitizers (ATWDs) digitize the PMT waveform with fine-binned timing resolution, and a fast analog to digital converter (fADC) digitizes the waveform with coarse timing resolution.

A photo-multiplier tube (PMT) is an extremely sensitive detector of light, including a photo-cathode with a very low work function, so that even visible light photons can eliberate electrons from the cathode material. In the base of the PMT, there is a series of dynodes, with a very high potential (typically $\sim$ 1200 Volts) with respect to the photocathode.

The high potential of the first dynode accelerates the knocked out electron towards the dynode chain. It then strikes the first dynode with enough energy to liberate a few more electrons itself. The result is a large amplification in the number of electrons so that a final current can be measured. The final current is proportional to the number of photo electrons emitted.

When the signal of the PMT exeeds a defined threshold (typically 0.3 photo electrons) the waveform is captured and digitized, if a local coincidence occurs. This condition requires a DOM and its nearest neighbors having a readout event within $\pm$1000 ns. The local coincidence condition should suppress isolated noise hits in the detector.

The data acquisition system (DAQ) is a collection of hardware, firmware and software components for acquiring data from the DOMs and assembling the DOMs readouts into events based on the trigger criteria. The DOM calibration is performed with the program *domcal* which is running on the DOM itself. After the electronics of the DOM are calibrated the PMT's response to single photoelectrons has to be calibrated as well. The ATWD waveforms do not have any calibration applied when they come from the detectors output. This calibration is applied offline during the reconstruction of the event.

There are various trigger conditions that can be used for the selection of events in the detector. For the purpose of this analysis one is important. The in ice **simple majority trigger** (SMT) requires that 8 DOMs are read out and transimitted to the surface with their hits occuring in a $5\,\mu s$ time window. All DOM readouts in a $16\,\mu s$ window around the trigger window are furhter included in the constructed event. The trigger window is defined so that any signal in IceTop associated with the event is contained within.
The rate of events in IC-22 satisfying this trigger is 342 Hz.
The DAQ outputs approximately 75 GB/day, for all triggers currently implemented [Ice]. Though the data rate is quite modest on the scale of typical particle physics experiments, it is much larger than the bandwidth that can be used for IceCube from the Pole, which requires that all data must fit over approximately 4GB/day satellite bandwidth. That means in reverse that over 90 % of the data volume must be rejected at the Pole and only the physically interesting events are sent north. To do so a processing and filtering computer cluster is running at the Pole to reconstruct the events on a number of criteria required for different analyses. Several filters are then applied on the simple reconstructed events and the filtered data is finally transmitted to the North.
For this work, the filter stream of interest is the up-going muon filtering scheme. It attempts to select events which seem to be up-going. Because there is also limited processing time at the Pole, two fast first-guess reconstructions, namely a linefit and a dipolefit are applied to determine whether the event should be kept or rejected. See chapter 5 for a detailed description of reconstruction methods. The up-going muon filter requires either the linefit or the dipolefit to reconstruct the event with a zenith angle greater than Θ_{cut}, as well as the event having $nHit_{cut}$ or more DOMs hit.

4

Simulation

The simulation of events in the detector provides a crucial basis for nearly every analysis done in IceCube. Already the reconstruction of the muon's track from measured observables has simulated data, implemented in its framework. For further data analyses the comparisons between the simulated and experimental data is the starting point for calculations and applications. For the named reasons the purpose of this chapter is to give an introduction to the simulation framework in IceCube.

The simulation chain consists of six consecutive elements:

- **Generation** As a first step in simulation the interactions of the primary particles, either cosmic rays or atmospheric neutrinos, are simulated up to the point at which they produce muons that might be observed in the detector. As a result a set of muons which potentially may trigger the detector is generated.
- **Muon Propagation** The generated muons are further propagated through the matter of the Earth until they have lost all their energy and finally decay. The focus of the simulation at this stage lies in the different energy loss processes of the muon.
- **Photon Propagation** The propagation of the emitted Čerenkov photons in the ice of the detector is computed using pre-calculated tables that contain the resulting photo electron density and expected photo electron arrival time probability density functions (pdfs) at each DOM. They depend on the detector depth and are called photonics tables.
- **PMT Simulation** Expecting a certain amount of photons arriving at a DOM, the

simulation of the PMT response is done which results in a set of waveforms for each of the simulated events.

- **DOM Simulation** The subsequent capture by the DOMs hardware components ATWD and fADC are simulated accounting for the local coincidence condition between neighboring DOMs.
- **Trigger Simulation** As a final step the various trigger requirements have to be applied to the resulting simulated events.

4.1 Generators

4.1.1 Neutrino Event Generator

The neutrino event generator NuGen is used for the simulation of neutrino induced events in the IceCube detector. The considered neutrino events are of two classes which only differ in the shape of their fluxes, namely atmospheric and astrophysical neutrinos. Both are therefore generated simultaneously and are weighted afterwards according to a certain flux expectation model. The primary neutrinos are injected following a hard E^{-1} or E^{-2} energy spectrum at the surface of the Earth. Once the neutrino is propagated through the Earth and reaches the detector depth the interaction of the neutrino via different interaction channels is simulated. A neutrino or a charged lepton and/or hadrons are generated according to the existing interaction probabilities. These probabilities are stored as a weight which is assigned to every event. The weight can further be used to reweight the events according to a certain flux prediction.

4.1.2 CORSIKA Air Shower Generator

CORSIKA is a software simulating extensive air showers produced by cosmic rays in the atmosphere [WBB$^+$03].

The program simulates the generation of protons and heavier nuclei at the top of the atmosphere and propagates them down to the surface of the Earth. The generated air showers contain muons and neutrinos, which are further propagated through the ice to the location of the detector. The standard CORSIKA program has been modified to account for the curvature of the atmosphere which affects muons traveling at high zenith angles [Chi04]. Two different models are implemented to describe the hadronic interactions of the primary cosmic rays, namely QGSJET01 [Ke91], for high energetic hadrons and GEISHA [Fes85] for low energetic hadrons.

4.2 Propagation

The propagation of the generated muons from the surface down to and through the detector is calculated by the Muon-Monte-Carlo (MMC) [CR04]. MMC divides the energy loss processes of muons in a stochastic and a continuous component. All energy loss processes in which secondaries below $E_{cut} = 0.5\,\mathrm{GeV}$ are produced are assigned to be continuous, while all other processes are considered to be of stochastical nature. The MMC determines the point at which the stochastic energy loss events occur and what kind of interaction, either pair production, bremsstrahlung or photo-nuclear interaction, is involved (see section 3.1.1 for a more detailed description of the energy loss of muons in ice).

The calculations of the various energy loss mechanisms are accurate within about 1% for muons less than 1 TeV [CR04]. As a result MMC provides information about the area along the muon track where the energy loss happens continuously and at which points on the track the energy is lost due to an electromagnetic cascade.

The propagation of the emitted photons is done by using the photonics tables mentioned above. Photonics is a simulation software that calculates the photon flux density in ice, through a surface which is surrounding a specified light source by taking in consideration the depth dependent ice properties of the antarctic glacier [Mio01]. The full depth profile (in 10 m bins) of scattering and absorption is stored in tables so that the photons can be tracked through a specified simulation volume after they have been generated. During the propagation process, a weight is assigned to the photon defining its survival probability at this stage. This is done by using a function of the absorption length which depends on the wavelength. After this step of simulation is performed, multidimensional tables for either a point like source (electromagnetic shower) or for muon track segments are generated containing photon densities and arrival time distributions for photons. For each light source position and its orientation one table is generated.

For a specific event, the locations and orientations of light generating subevents, like electromagnetic showers, are obtained by MMC. The locations of the DOMs are forwarded through the simulation. By using the additional pieces of information from the photonics tables, the time distributed number of photons at each DOM is finally obtained for each event [LMW+07].

4.3 Hardware Simulation

After obtaining individual photo electron arrival time distributions from photonics the root-based optical module emulator (ROMEO) simulates the corresponding charge measured by a PMT, superimposing a sequence of a Gaussian distributed voltage pulse to each photo electron arrival. The resulting waveform serves as the input for the DOM mainboard simulation, which consists mainly of the ATWD and fADC waveform capture simulation. This can be regarded as an *decalibration* of the waveform. At this point the local coincidence requirement is taken into account by the simulation and further trigger conditions are applied. Events are considered to have triggered the detector if they have more than 8 readouts in a $5\,\mu s$ time window. Eventually all readouts in a $16\,\mu s$ time window are assembled to present the final event.

5

Reconstruction Techniques

The reconstruction of an event observed in the detector is vital for every data analysis. Several algorithms have been developed to improve the quality of the reconstruction with respect to the angular resolution of the track's direction. The reconstruction is performed in different steps. The first step is done by application of a first guess algorithm. This is followed by a more complex reconstruction algorithm, the logarithm-likelihood method, (see sec. 5.3) to gradually improve the reconstructed parameters. The purpose of this chapter is to give a general introduction into the different reconstruction methods followed by an overview of the derived parameters.

5.1 Hit Preparation

Before starting with the actual reconstruction one has to remove all hits that are obviously not part of the muon event being reconstructed, or that stem from malfunctioning DOMs. This is done by cleaning out all readouts that occur on a pre-defined list of bad DOMs. It takes place in the software processing chain.
A typical calibrated waveform captured by a DOM is shown in Fig. 5.1.

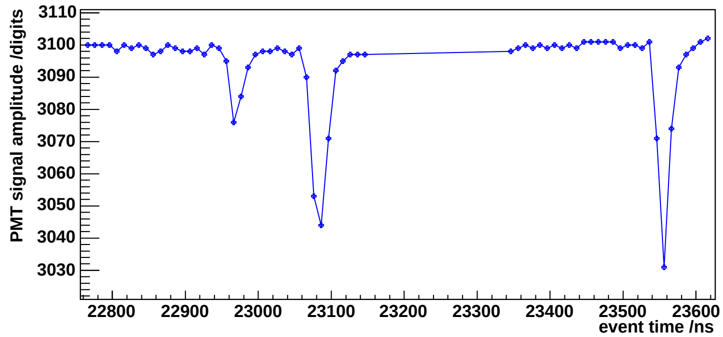

Figure 5.1: Typical waveform of an OM. [Wag04]

The different features of the waveform, such as time, amplitude, width and area of the primary and secondary pulses can now be used for the reconstruction of the energy and track of the muon. An algorithm called *feature extractor* extracts single photon hit times by iteratively fitting the waveform with a function that is the sum of a constant and progressively larger number of terms, each describing a single photo electron response of the PMT. It is given as:

$$F^n(t) = b_0 + \sum_{k=1}^{n} A^k \mathrm{f}\left(\frac{t - t^k}{\delta^k}\right), \tag{5.1}$$

where b_0 is the baseline estimate, A^k, t^k and δ^k are respectively the amplitude, time and width of the kth pulse. The function $\mathrm{f}(\zeta)$ is the single photo electron (SPE) waveform. The application of the feature extractor provides two forms of the fitted waveform, namely a series of single photo electron arrival times, or "Reco Hits" and a series of extracted waveform pulses, or "Reco Pulses". The latter has a leading edge time, a total charge and a width. Both are useful for reconstruction.

This method provides a resolution of the photon arrival times within 0.5 ns.

A *time window hit cleaning* then extracts a time window of $4\,\mu s$ of the DOM readouts in which the maximum number of hits occur. Since the time, the muon spends within the detector volume, is at maximum $3\,\mu s$ the chosen time window only preserves physically reasonable hits and coevally rejects hits, which are most probably random noise. The same purpose has *isolated hit cleaning* which requires coincidental hits within 100 meters and 500 ns.

5.2 First-guess Reconstruction Methods

The first-guess reconstruction methods serve two purposes in the overall reconstruction process. First they are a fast and effective way of reducing the data output at the Pole by rejecting events which are primarily reconstructed as downgoing. Second they serve as a seed for the more complex and resolutive likelihood reconstruction algorithms. The named methods are the line fit and dipole fit which are explained in the following sections.

5.2.1 Line Fit

The line fit algorithm computes an initial track using the information of the hit times at each PMT. It totally ignores the geometry of the Čerenkov cone as well as the optical properties of the ice and assumes a plane light wave moving with a velocity v through the detector. The locations of each PMT, r_i, being hit at a time t_i are connected by a line as follows:

$$r_i \approx r + v \cdot t_i. \tag{5.2}$$

A χ^2 fit is further done defined as:

$$\chi^2 = \sum_{i=1}^{N_{hit}} (r_i - r - v \cdot t_i)^2, \tag{5.3}$$

where N_{hit} is the number of hits. This equation can be minimized analytically yielding:

$$r = \langle r_i \rangle - v \cdot \langle t_i \rangle \tag{5.4}$$

and

$$v = \frac{\langle r_i \cdot t_i \rangle - \langle r_i \rangle \cdot \langle t_i \rangle}{\langle t_i^2 \rangle - \langle t_i \rangle^2}. \tag{5.5}$$

The line fit produces a vertex point r and a direction e, given by $e = v_{LF}/\,|v_{LF}|$, of the reconstructed track. While the absolute speed $v_{LF} = |v|$ of the line fit is the average speed of the light propagating through the one-dimensional detector projection. Spherical events like cascades and high energy muons have low values of v_{LF}, whereas *thin*, long events, that means minimally ionizing muon tracks, have larger values of v_{LF}. Thus the line fit speed can be further used for the classification of events in the detector. The zenith angle of the track's direction is finally given as: $\Theta_{LF} = \;\; - \arccos(v_z/\,|v_{LF}|)$.

5.2.2 Dipole Fit

The dipole algorithm considers the unit vector from one hit DOM to the subsequently hit DOM as a dipole moment. Averaging over all individual dipole moments gives the total dipole moment $\mathbf{M}$ which in turn gives the direction of the reconstructed track.

$$\mathbf{M} = \frac{1}{N_{ch} - 1} \sum_{i=2}^{N_{ch}} \frac{r_i - r_{i-1}}{|r_i - r_{i-1}|}, \tag{5.6}$$

where N_{ch}) is the number of hit OMs, or number of (hit) channels, and r_i are their positions. Though the dipole fit does not provide results as good as the linefit, it is not as susceptible to coincident atmospheric muon events, in case that one event occurs at the top of the detector volume and the coincident second at the bottom.

5.3 Maximum Likelihood Fit

As the method of maximum likelihood is a common technique used to estimate a set of unknown parameters $\mathbf{a}$ from a set of independent measured values $\mathbf{x} = \{x_i\}$ it can - with some modifications - also be used in the context of reconstructing muon tracks. The method proceeds by first forming a likelihood function $\mathcal{L}$ given as:

$$\mathcal{L}(\mathbf{x}|\mathbf{a}) = \prod_i \mathrm{p}(x_i|a_i), \tag{5.7}$$

where $\mathrm{p}(x_i|a_i)$ is the probability density function (pdf) of observing the measured value x_i for given values of the parameters $\mathbf{a}$. The task of the likelihood fit is to identify the parameters $\mathbf{a}$ that maximize the value of $\mathcal{L}(\mathbf{x}|\mathbf{a})$. In practice the reconstruction is done by minimizing $-\log \mathcal{L}$ which is mathematically equivalent but easier to work with since the used values are very small.

The parameters that specify a muon track are its position x, y, z and time t along the track as well as the zenith angle Θ and the azimuth angle ϕ of the direction the muon is approaching from. To keep the likelihood function a function of only five parameters the time t of the vertex is assumed to be a constant value. The measured values x_i are the position of the hit OMs in the detector and the arrival times of the recorded photons.

All the physics is contained in the choice of the pobability density function $\mathrm{p}(x_i|a_i)$. From AMANDA, the Antarctic Muon And Neutrino Detector Array, a likelihood function has been adopted that gives the probability of observing a set of hit times given a certain hypothesis, while the so called Pandel function [Pan96] serves as a pdf. The original AMANDA data aquisition system recorded only the leading edge time of the photomultiplier pulse, the total charge of the pulse and the total time over threshold of the pulse. In IceCube there are two further strategies to do reconstruction by minimization of the log-likelihood function both using the complete waveform recorded by a DOM. The one uses the waveform as a whole while the other uses the extracted photon arrival times from the waveform given by the feature extractor [GBH08].

5.3.1 Pandel likelihood

The likelihood which gives the probability of observing a set of hit times assuming a certain hypothesis is written as:

$$\mathcal{L}_{\mathcal{P}\dashv\backslash\sqcap\updownarrow}(hits, \mathbf{x}) = \prod_{i}^{N_{hits}} \mathrm{p}(t_{res,i}|\mathbf{x}) \tag{5.8}$$

and is equal to the product over the probabilities from individual arriving times coming from the hypothesis in question. A hit is defined as the arrival time of a single Čerenkov photon at an OM, triggering a photo electron. In this case the residual time of the hits are rather used within the likelihood function than the hit times themselves.
A residual time is defined as the difference of the observed hit time and the expected hit time for a *direct* photon, which has not been scatterd on its way to the OM. Given the variables defined in Figure 5.2 for a certain track hypothesis it is:

$$t_{geo} = t_0 + \frac{\hat{\mathbf{p}} \cdot (\mathbf{r}_i - \mathbf{r}_0) + d \cdot \tan(\Theta_0)}{c}, \tag{5.9}$$

where c is the vacuum speed of light. This is the simplest form of the equation made under the assumption that the phase and group velocity of light in ice are the same. With the definition of t_{geo} the residual time t_{res} writes:

$$t_{res} \equiv t_{hit} - t_{geo}, \tag{5.10}$$

where t_{hit} is the time of the photon hit. For each measured hit in the detector one can assign a residual time t_{res} for that hit given a hypothesis $\mathbf{a}$. Further assuming that the distribution of t_{res} depends on the distance d_i of the muon track from the OM and the angle η_i between the Čerenkov cone and the axis of the PMT, the function $\mathrm{p}(x_i|a_i)$ then becomes a function of three parameters, t_{res}, d_i and η_i.

The pdf which parametrizes the arrival time distribution of Čerenkov photons as a gamma distribution is the Pandel function [Pan96]. By means of simplification clear ice, without dust layers, has been assumed for its alignment. The Pandel function is defined as:

$$\mathrm{p}(t_{res}) \equiv \frac{1}{N(d)} \frac{\tau^{-(d/\lambda)} t_{res}^{(d/\lambda - 1)}}{\Gamma(d/\lambda)} e^{-(t_{res}(\frac{1}{\tau} + \frac{c_{medium}}{\lambda_a}) + \frac{d}{\lambda_a})}, \tag{5.11}$$

where λ_a is the absorption length, d is the closest approach distance between the DOM location and the hypothesis. λ and τ are two unspecified parameters whose form depends on whether the hypothesis is based on a muon track or a track of an electromagnetic cascade.

Before minimizing the log-likelihood term the first guess method from section 5.2 or a Sobol seed is performed to generate a list of hypotheses for **a**. This is done by sampling the parameter space for **a** systematically. The Sobol sequence is an algorithm that generates a pseudo-random sequence of numbers i.e. it uniformly samples a space rather than randomly sampling it. For each of the selected hypotheses a numerical minimizer algorithm is finally applied to determine the minimum.

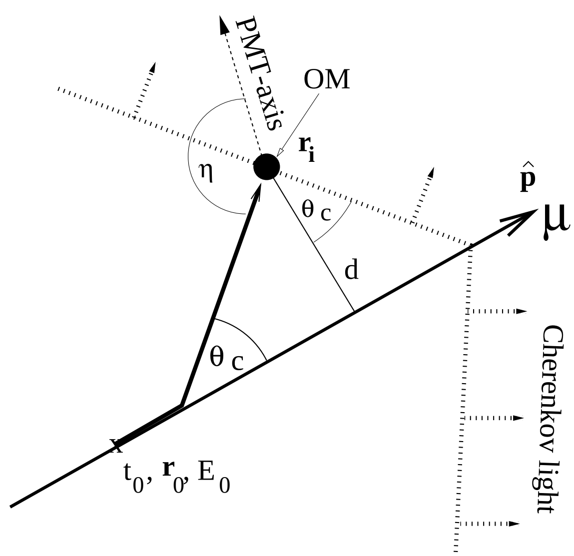

Figure 5.2: A schematic illustration of the muon track geometry. [Wie]

5.3.2 Waveform Based Log-Likelihood Reconstruction

The log-likelihood function based upon the complete waveform is derived from the probability of observing a waveform f(t) given an expected photo electron distribution $\mu(t)$ in the PMT. While the waveform is obtained by measurement and the expected photo electron arrival time distribution is contained in the pdf. The pdf depends on different hypothetical parameters, like the position $\mathbf{x}$ of the muon at time t_0, the direction of the muon track and its energy E. It is set up by assuming a Poissonian distribution for the probability of observing n_i photons in the ith waveform bin, given an expectation of μ_i photons in the same ith waveform bin. The total probability for a waveform recorded in a single DOM is then given by the product over all waveform bins as [GBH08]:

$$\mathcal{L}(\mathrm{f}(t)|\mathbf{x}, E) = \prod_{i=1}^{K} \frac{e^{-\mu_i}}{n_i!} \mu_i^{n_i}. \tag{5.12}$$

Rearranging this equation gives:

$$\mathcal{L}(\mathrm{f}(t)|\mathbf{x}, E) = \left(\prod_{i=1}^{K} \frac{\mu_i^{n_i}}{n_i!} \right) \left(\frac{\prod_{i=1}^{K} \mu_{tot}^{n_i}}{\prod_{i=1}^{K} \mu_{tot}^{n_i}} \right) \left(\prod_{i=1}^{K} e^{-\mu_i} \right), \tag{5.13}$$

and finally:

$$\mathcal{L}(\mathrm{f}(t)|\mathbf{x}, E) = N_{pe}! \prod_{i=1}^{K} \frac{\left(\frac{\mu_i}{\mu_{tot}}\right)^{n_i}}{n_i!} \frac{\mu_{tot}^{N_{pe}}}{N_{pe}!} .e^{-\mu_{tot}} \tag{5.14}$$

This form of the likelihood gives the probability that N_{pe} photo electrons are exactly arranged into K bins of the waveform multiplied by the Poissonian probability of these N_{pe} photo electrons occurring at a PMT. The logarithm of the likelihood gives the sum over all K bins as follows:

$$\log \mathcal{L}(\mathrm{f}(t)|\mathbf{x}, E) = \sum_{i=1}^{K} \left(n_i \log \frac{\mu_i}{\mu_{tot}} \right) + N_{pe} \log \mu_{tot} - \mu_{tot} - \sum_{i=1}^{K} \log(n_i!). \tag{5.15}$$

Each term in the first sum corresponds to the logarithm of the probability of observing a photoelectron in the ith waveform bin at time t_i weighted by the total number of observed photo electrons in the ith waveform bin, or just p_i. The second and third term of the equation only depends on the total number of observed photo electrons μ_{tot} and is therefore used to reconstruct the energy of the muon.

The obtained log likelihood function is then maximized with respect to the free parameters of the muon track by fitting the shape of the pdf to the measured waveform.

This allows the reconstruction of not only the muon track but also of its energy.

5.3.3 Feature Extractor Based Log-Likelihood Reconstruction

After the feature extractor is applied to the measured waveforms one obtains either a series of single photoelectron arrival times ("reco hits") or a series of extracted waveform pulses ("reco pulses") (see Section 5.1). The feature extractor based log-likelihood then uses the probability of observing a set of reco hits or reco pulses t_i, given an expected photo-electron distribution μ_t. It can be noted down in the form of:

$$\log \mathcal{L}(\mathrm{f}(t)|\mathbf{x}, E) = \sum_{i=1}^{K} (n_i \log \mathrm{p}(t_i|\mathbf{x})) + N_{pe} \log \mu_{tot} - \mu_{tot} \tag{5.16}$$

Now all reco hits and reco pulses are summarized, while n_i is the charge of a reco pulse ($n_i = 1$ reco hits) and N_{pe} and μ_{tot} are the total measured and expected charges respectively. In analogy to equation 5.3.2 $\mathrm{p}(t_i|\mathbf{x})$ is the normalized probability of a single photo electron arriving at a DOM at time t_i.

5.3.4 Bayesian Fit

The Bayesian fit is a likelihood algorithm used to test the hypothesis that the muon track is down-going, though it is reconstructed as up-going by the standard likelihood approach [Hil01]. A method adopted from Bayesian statistics is applied in that the likelihood is weighted by a prior probability describing the origin of the particle. The probability $P(\vec{\mu}|\mathcal{H})$ that a muon track $\vec{\mu}$ is responsible for a hit pattern $\mathcal{H}$ can then be expressed as:

$$P(\vec{\mu}|\mathcal{H}) = P(\mathcal{H}|\vec{\mu}) \frac{P(\vec{\mu})}{P(\mathcal{H})}, \tag{5.17}$$

where $P(\vec{\mu}|\mathcal{H})$ is the probability to find a hit pattern $\mathcal{H}$ assuming a muon track $\vec{\mu}$.

5.4 Levels of Reconstruction

5.4.1 Level 0

At level 0 of the reconstruction chain the raw data is simply converted from the processing and filtering format (P&F) to the standard offline format, namely ".i3" files. In addition, geometry, calibration and detector status streams are obtained from the database.

5.4.2 Level 1

The level 1 process is run on the resulting .i3 files from level 0 processing. At level 1 only events that satisfy either the in ice multiplicity trigger, the upgoing muon trigger or the high multiplicity trigger are selected. These three kinds of data are further split up into the "minibias", "upmu" and "ehe" folders, respectively. After these events have been selected, basic reconstruction algorithms, like line fit, dipole fit and a single seeded log-likelihood are run on them, before information of bad DOMs is filtered out. Further on, the DOM calibrator is executed which creates calibrated waveforms from whom the feature extractor extracts hits. For each event the first hit on each DOM is used for the reconstructions, where only those hits are used that occured in a predefined time window of $4\,\mu s$.

5.4.3 Level 2

The main goal of level 2 processing is to provide a standard high level reconstruction of the events. No event selection or filtering will be executed during this process. Several steps are proceeded to reconstruct muon tracks from the available event information of the preceding reconstruction processes. The steps are described below.

Log-Likelihood Reconstruction

A log-likelihood reconstruction using a convoluted Pandel function is performed in order to find the best track for an upgoing muon event and to get a first rejection of misreconstructed downgoing muons. The likelihood is run with 32 seeds provided by the sobol seed as well as by the line fit and dipole fit.

Paraboloid Fit

In the next step a paraboloid fit is executed on the likelihood space around the reconstructed track minimum. The paraboloid fit evaluates the likelihood function in the neighborhood of the best fit and constructs a parabola to the shape of the likelihood. The minimum of this parabola is used as the paraboloid fits best estimate of the tracks direction, whereas the width of the parabola provides an estimate of the angular uncertainty for each event.

Bayesian Reconstruction of Downgoing Muons

After the current iterative reconstruction the same events are again reconstructed using a predefined weight, forcing all tracks to originate in the hemisphere above the horizon. The purpose of this reconstruction is to allow a distinction between properly and misreconstructed tracks by comparing the respective likelihood values. The purpose of this step is to provide parameters for the efficient reduction of misreconstructed downgoing muons.

Double Muon Reconstruction

In this step the same log-likelihood reconstruction is done as in the previous steps but this time based on a coincident downgoing muon event. This is done by splitting the series of measured hits into two parts and reconstruct both parts apart. This step also provides parameters for a reduction of misreconstructed coincident muon events.

5.4.4 Level 3

At level 3 a first selection on events is performed which passed the muon filter and have a zenith angle above 80° calculated by a first iterative log-likelihood reconstruction. So done the event rate is lowered from 20.7 Hz passing the muon filter to ~ 7 Hz. Another cut is done on parameters of the 34-seed log-likelihood fit. Again events which reconstruct with a zenith angle less than 80° as well as a reduced log-likelihood (rlogl) value (see section 6.2) larger than 13 are rejected. All other events are contained in the 'level 3' dataset which is still dominated by events which are actually down-going but are falsely reconstructed as up-going. This datasample with high quality reconstructions is generally applicable to point source, atmospheric and diffuse neutrino analyses.

6

Analysis Procedure

6.1 Overview of the Analysis Chain

The final goal of the analysis is to reconstruct the atmospheric neutrino energy spectrum from the measured data of the year 2007. To ensure the *blindness* of the analysis an isotropically distributed sample of 20 % of the provided data files is used.

The analysis chain is constructed to achieve a pure atmospheric neutrino sample from the provided level 3 reconstructed dataset (see 5.4.4). Two different methods are applied to separate the atmospheric neutrino signal from background. They are optimized in terms of obtaining a preferably high signal efficiency as well as a high background rejection. The mis-reconstructed background events that survive up to level 3 are typically of a relatively poor quality and can therefore be removed with adequate quality cuts. A significant part of these mis-reconstructed events are muons that enter the detector coincidentaly from the bottom and the top. This additional class of background events needs closer examination. The procedure is first done by a graphical cut analysis selecting reconstruction parameters which can provide information about the quality of the reconstruction and serve as a classifier. A set of cut values is chosen to maximize the number of detected upgoing events while maintaining a purity of at least 95 %. A second approach is performed by using a decision tree algorithm, the Random Forest, as a classifier to effectively separate signal from background. Also in this case, the cut on the output is chosen to optimize both signal efficiancy and background rejection.

6.2 Determination of the Cuts

The step of this analysis procedure is to cut away low-quality up going events and to remove any contamination by downgoing muons. As a starting point, level 3 processed simulated, as well as experimentally measured datasets are chosen.
The following section will give a brief overview of the parameters used in further analysis:

- **Number of Direct Hits** (NDirC)

  The NDirC is defined as the number of hits of photons that arrive within a time window of -15 to 75 ns. The time window is derived from the expected time of a non-scattered Čerenkov photon which has been emitted from the reconstructed muon track and arrives at the DOM. Only the first photon hits are used for the calculation. This condition suggests that the hit arrives with less scattering and therefore provides more reliable information about the track's geometry. An event with a large number of direct hits has a higher quality than an event with only a few direct hits. This paramter is very powerful in identifying well reconstructed tracks and to reject coincident downgoing muons, but has to be used with caution. Since the intervals between the strings are 125 m apart, which is four times larger than the typical scattering lenght of photons in ice, even a high energetic neutrino event may fail to generate enough direct hits to survive the NDirC cut.

- **Direct Length** (LDirC)

  The direct length of the event is obtained by projecting each of the direct hits onto the reconstructed muon track (Figure 6.1) and by taking the distance between the outermost of these points. This corresponds to the lever arm of the reconstruction, whereas larger values correspond to a more precise reconstruction of the track's direction. A long direct length represents a high-quality event.

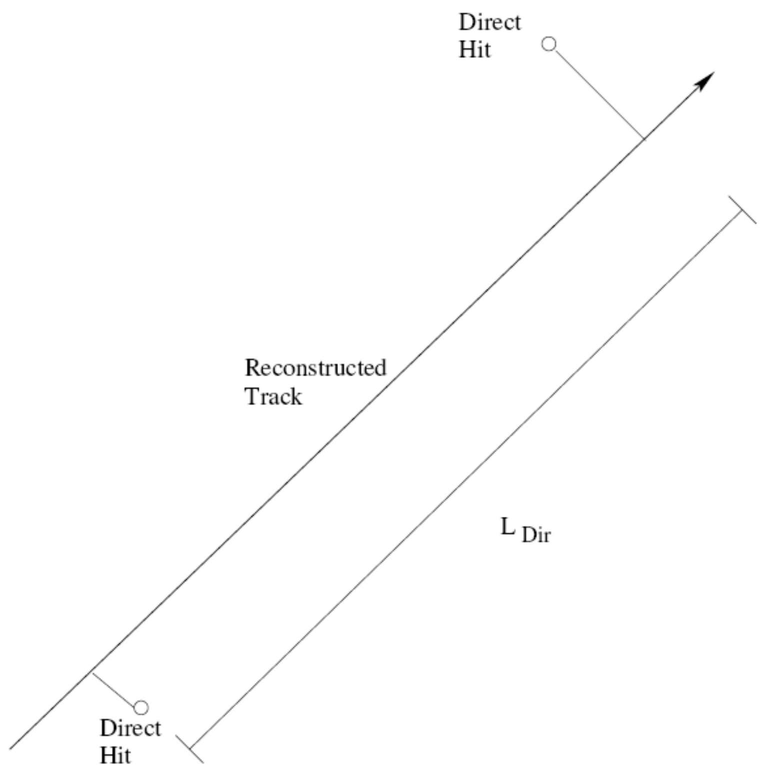

Figure 6.1: Illustration of L_{dir}. Direct hits are projected onto the reconstructed muon track. The distance between the outermost of these points is the direct length [Pre06].

- **Paraboloid Sigma** (sigma)

  The value of sigma for each event is defined in terms of the paraboloid error ellipse estimates for the major and minor axes **x** and **y** as follows:

$$\sigma = \sqrt{(\sigma_x^2 + \sigma_y^2)/2} \tag{6.1}$$

  The values σ_x and σ_y are determined by the paraboloid fit, which fits the likelihood space around the reconstructed track minimum. The paraboloid sigma fit is a good and robust reconstruction of the angular uncertainty of an event and shows a good background rejection power as well as the capability to select well reconstructed tracks.

- **Reduced Log-Likelihood** (rlogl)

  The reduced log-likelihood is defined as the value of the likelihood reconstruction divided by the number of degrees of freedom (dof) of the fit. The number of dof is taken to be the number of hit DOMs minus 5, the number of parameters of a track fit. A smaller value indicates that the emitted photons arrive as predicted by the convoluted Pandel function.

- **Bayesian Weighted Log-Likelihood - Pandel Log-Likelihood** (Likelihood Difference)

  The likelihood difference compares the best likelihood value to a likelihood value calculated using the down-going muon zenith distribution as Bayesian prior. The cut parameter is calculated as the ratio of the best fit likelihood to the Bayesian likelihood. Higher values are an indication that the event is most likely upgoing. This parameter identifies mostly atmospheric muons which are wrongly reconstructed as upgoing tracks in the horizontal region.

- **Umbrella Likelihood Ratio** (Llh Ratio)

  Similar to the Bayesian weighted likelihood an *umbrella* fit is performed by constraining the fit to the opposite hemisphere. If the likelihood value of the fit is similar to the best fit of the likelihood value based on the pandel function we have an indication that the event direction is not well constrained. On the other hand there is confidence in the initial likelihood reconstruction if the value is worse.

- **Smoothness**

  The Smoothness is a measure of the consistency of the observed hit pattern with the hypothesis of a constant light emission by a muon. Each hit is projected on the reconstructed track as illustrated in Figure 6.2. The Smoothness is then given as [The04]:

  $$S_j \equiv \frac{j-1}{N-1} - \frac{l_j}{l_N}, \tag{6.2}$$

  where l_j is the distance between points of closest approach to the first and jth hit module. N is the total number of hits. Tracks with hits clustered at the beginning or the end of the track have values of S approaching +1 or -1, respectively. Tracks that have hits equally spaced along the track, and therefore values of S close to zero, are reconstructed with a higher quality.

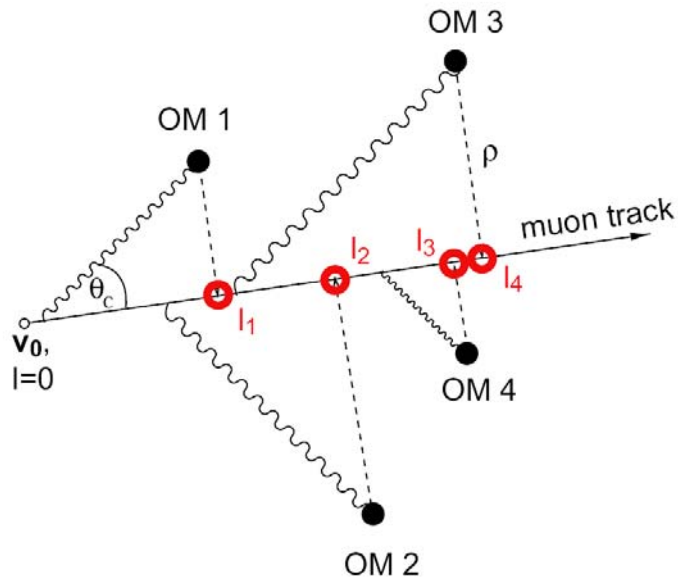

Figure 6.2: Illustration of the projection of the recorded hits on the reconstructed muon track. l_i denote the positions of the projected hits onto the muon track. More evenly distributed hits indicate a higher quality of the reconstruction [Ack06a].

- **Distance Length**(DisL)

  DisL denotes the distance from the closest point of the reconstructed muon track to the detector volume to the detector center. Tracks that hit the detector at its margin are of a poor reconstruction quality and often yield to mis-reconstruction.

6.2.1 Application of Cuts

For a comparison of the effects of the different cuts on background and signal weighted atmospheric neutrino Monte Carlos as well as Monte Carlos weighted with the astrophysical neutrino flux have been used.

The atmospheric neutrino flux is weighted based on the models by Honda (2006) for the conventional and by Naumov (RQPM) for the prompt flux. [HKK+06,FNV01]. The signal flux was assumed to be $5 \cdot 10^{-8}\,\mathrm{GeV\ sr^{-1}s^{-1}\,cm^{-2}}$ based on the determined flux limit by [Mue07] for the AMANDA 4-year analysis.

An analysis was first done on simulated samples with a livetime of 14 days to study several parameters on their reliability to provide information about the reconstruction quality and therefore to reject the two classes of background events. Simulated atmospheric single and coincident muons as well as simulated atmospheric and astrophysical neutrinos are used for comparison.

Subsequently a selected set of parameters as described above is used to accomplish the analysis on the 40.42 livetime datasample of the measured data as well as on simulated astrophysical and atmospheric neutrinos with the same livetime.

As the contamination caused by atmospheric muon events from just above the horizon is obvious, a cut on the reconstructed zenith angle is done at 90°. The remaining events constitute the level 4 sample which has been considered to be the starting point of the analysis.

Figure 6.6 shows the event distributions after the cut on the zenith angle has been applied. The NDirC parameter turned out to be the most powerful parameter to reject mis-reconstructed events and it is strongly suppressed, if the reconstructed track is entirely wrong. However, by applying straight cuts on NDirC, a part of the most energetic events originating mainly from the horizontal direction may disappear.

While the paraboloid sigma, and therefore a good zenith resolution, is essential to reject horizontal muon bundles, the correlation of both parameters has been studied.

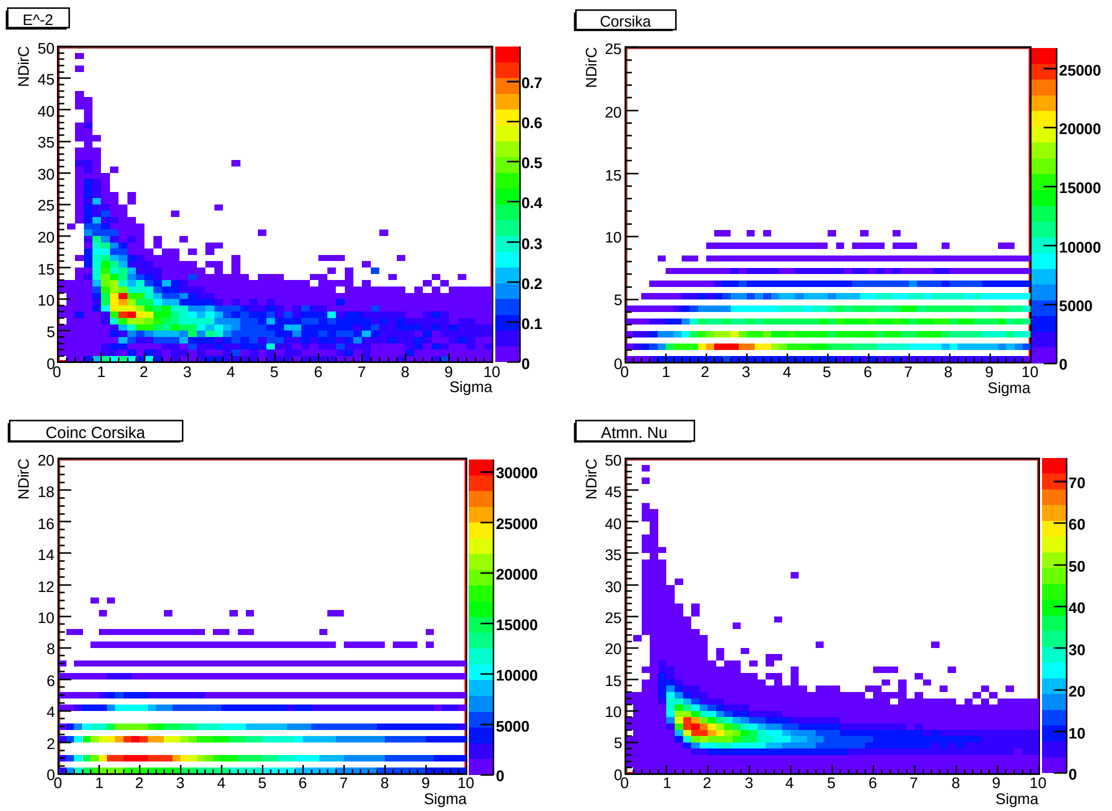

Figure 6.3: Two-dimensional correlation plot of the Number of Direct Hits (NDirC) within a time window of -15 to 25 ns against paraboloid sigma (zenith). On the top left: Simulated astrophysical neutrino events with an assumed spectral index of $\gamma = -2$. On the top right: Corsika simulated atmospheric muon events. On the bottom left: Corsika simulated coincident atmospheric muon events. On the bottom right: Simulated and weighted atmospheric neutrino events.

Figure 6.3 shows the NDirC distribution as a function of the paraboloid sigma in zenith direction. The largest peak of atmospheric muon background events is located between sigma $2-3°$ while the simulated atmsopheric and astrophysical neutrino event distributions show a peak around $1-2°$. In the case of the coincident atmospheric muon background events the peak position is close to those of simulated astrophysical and atmospheric neutrinos, but still noticeably over a value of $2°$. By comparing the simulated neutrino event distributions it can be clearly seen, when sigma decreases the values of NDirC increase.

These events with a high value of NDirC as well as a small angular deviation are well reconstructed tracks. At level 5, in order to reject only misreconstructed events, the cuts are applied, such that events with sigma larger than 2.2° or with a number of direct hits smaller than 19 are rejected:

- Paraboloid Sigma < 2.2 OR NDirC > 19

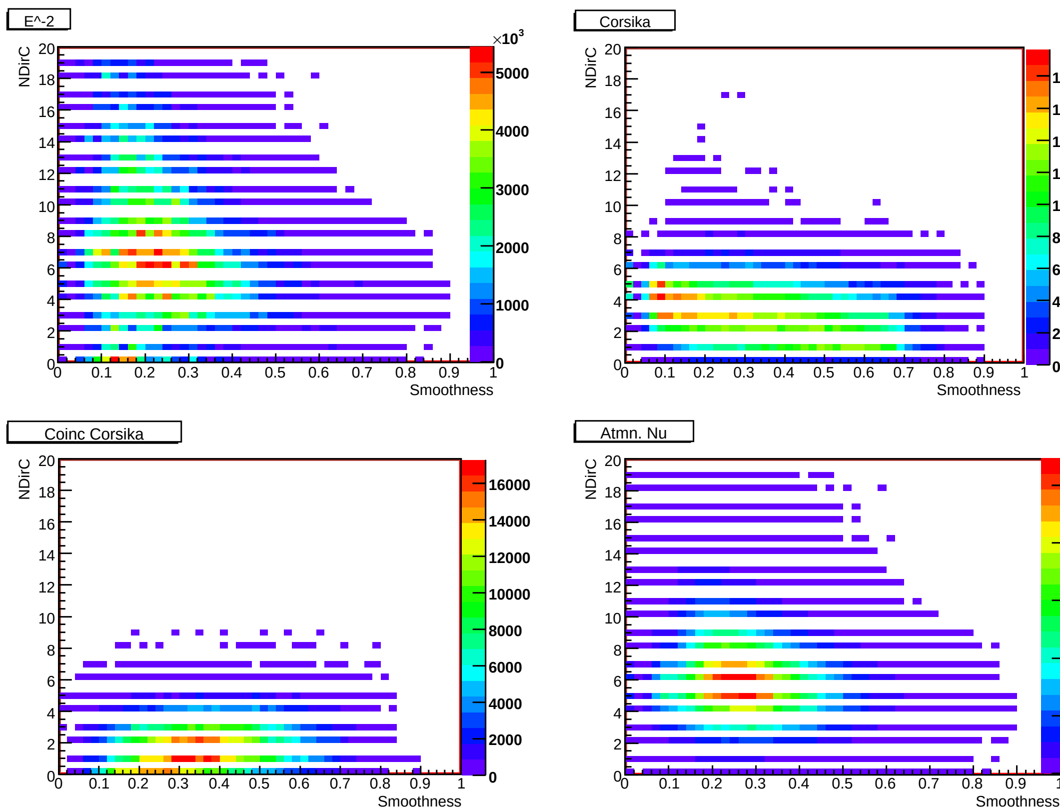

Figure 6.4: Two-dimensional correlation plot of the Number of Direct Hits (NDirC) against the track's smoothness. On the top left: Simulated astrophysical neutrino events with an assumed spectral index of $\gamma = -2$. On the top right: Corsika simulated atmospheric muon events. On the bottom left: Corsika simulated coincident atmospheric muon events. On the bottom right: Simulated and weighted atmospheric neutrino events.

Figure 6.7 shows the distributions after level 5 cuts have been applied. The signal neutrino flux is scaled up for a better illustration.

At this stage the datasample is still dominated by background events. Another cut was chosen on the absolute value of the smoothness at 0.35. Figure 6.4 shows the correlation between the absolute value of the track's smoothness and the number of direct hits. As can be seen, a cut on the absolute value of the smoothness at 0.35 rejects most of the misreconstructed coincident atmospheric muon events, while most of the atmospheric neutrino events can be preserved. After this cut $2.86 \cdot 10^6$ of all background events could be rejected. The remaining events make up the level 6 datasample.

After at level 7 a cut on the likelihood difference (Llh Diff) on values less than 20 has been applied, finally at level 8, a more tight NDirC cut is required to reject the remaining 39491.7 background events. To determine a optimal cut value for NDirC the different distributions for data and Monte Carlo are studied in the zenith angle-NDirC-plane as it is shown in Figure 6.5. The atmospheric muon events show two populations. Due to the fact that Corsika events cannot theoretically occur at high zenith angles the population at a lower cosine in Figure 6.5 must obviously be mis-reconstructed. This population can be rejected by a relative low cut on NDirC. The other population consists of horizontal events which have been reconstructed reasonably.

The following NDirC cut therefore is applied at level 8:

- NDir > 7

Figure 6.10 illustrates the distributions at cut level 8.

At the final cut level 9 additional cuts on LDir and DisL are executed. Table 6.1 shows the cuts, consecutively applied for level 1 up to level 9 together with the remaining background and signal events at each level.

At the final cut level 1274 events of measured data and approximately 1210 events of simulated atmospheric neutrinos have survived the cuts. The assumed number of backgroundevents therefore is 64. This is 5.02% of the remaining data sample at level 9.

Number of events at cut level				
cut level	**No. data ev.**	**No. atm. ν ev.**	**No. backgr. ev.**	**backgr. rej.**
level 4	$8.76285 \cdot 10^6$	5394	$8.7575 \cdot 10^6$	
level 5	$6.53269 \cdot 10^6$	5068	$6.527 \cdot 10^6$	25.46%
level 6	$3.66856 \cdot 10^6$	3866	$3.665 \cdot 10^6$	58.15%
level 7	$1.13937 \cdot 10^6$	3467	$1.1359 \cdot 10^6$	87.03%
level 8	41128	1636	$39.4917 \cdot ^3$	99.55%
level 9	1274	1210	64	99.9993%

Table 6.1: Number of remaining background and predicted atmospheric neutrino events after cuts have been applied at different levels as well as the background rejection factor.

All together the following cuts have been applied on the data set:

cut on parameters at cut level	
cut level	**applied cuts on parameters**
level 4	Reconstructed zenith $> 90°$
level 5	Sigma < 2.2 or NDirC > 19
level 6	Smoothness < 0.35
level 7	Llh Diff > 20
level 8	NDirC > 7
level 9	LDirC > 200 and DisL < 400

Table 6.2: Applied cuts on parameters at cut level

Figure 6.11 illustrates the distributions of data and Monte Carlo after all cuts have been applied. The total analysed dataset has a livetime of 40.42 days consisting of $9.53 \cdot 10^6$ events. After all applied cuts 1274 events survived the cuts. The signal efficiancy is 22.4 % with a background rejection of 99.9993 %.

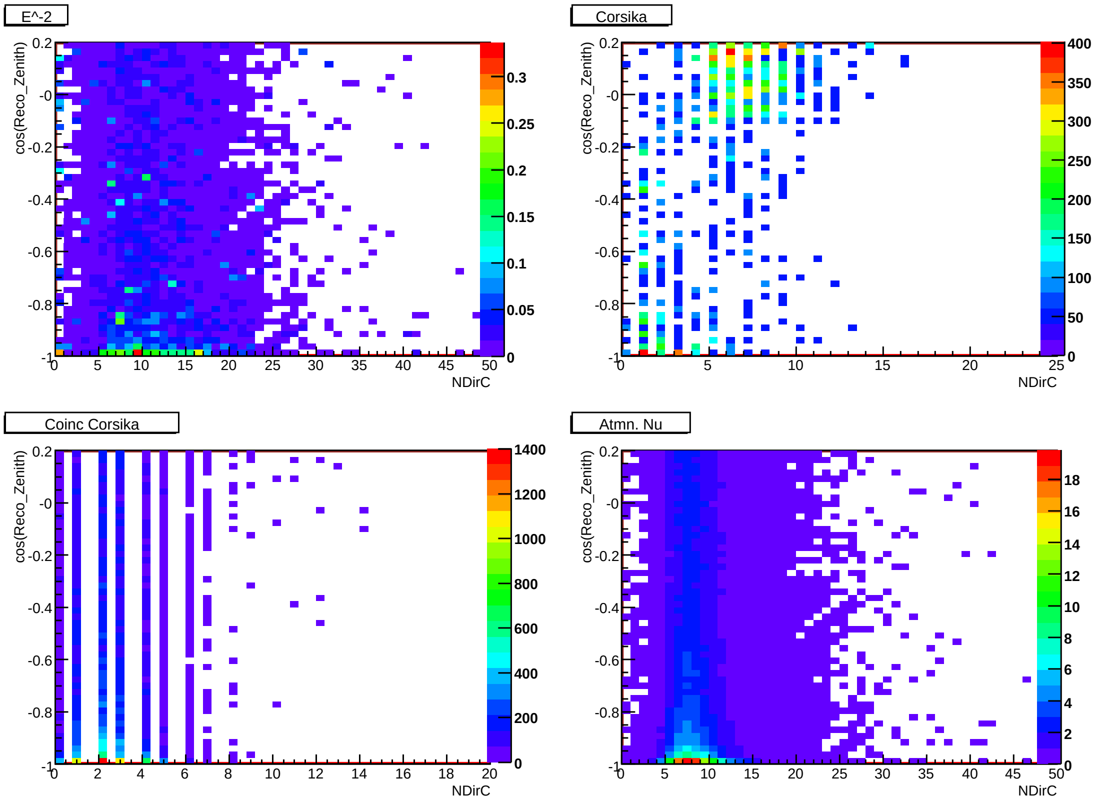

Figure 6.5: Two-dimensional correlation plot of cos(Reco Zenith) against NDirC. On the top left: Simulated astrophysical neutrino events with an assumed spectral index of $\gamma = -2$. On the top right: Corsika simulated atmospheric muon events. On the bottom left: Corsika simulated coincident atmospheric muon events. On the bottom right: Simulated and weighted atmospheric neutrino events.

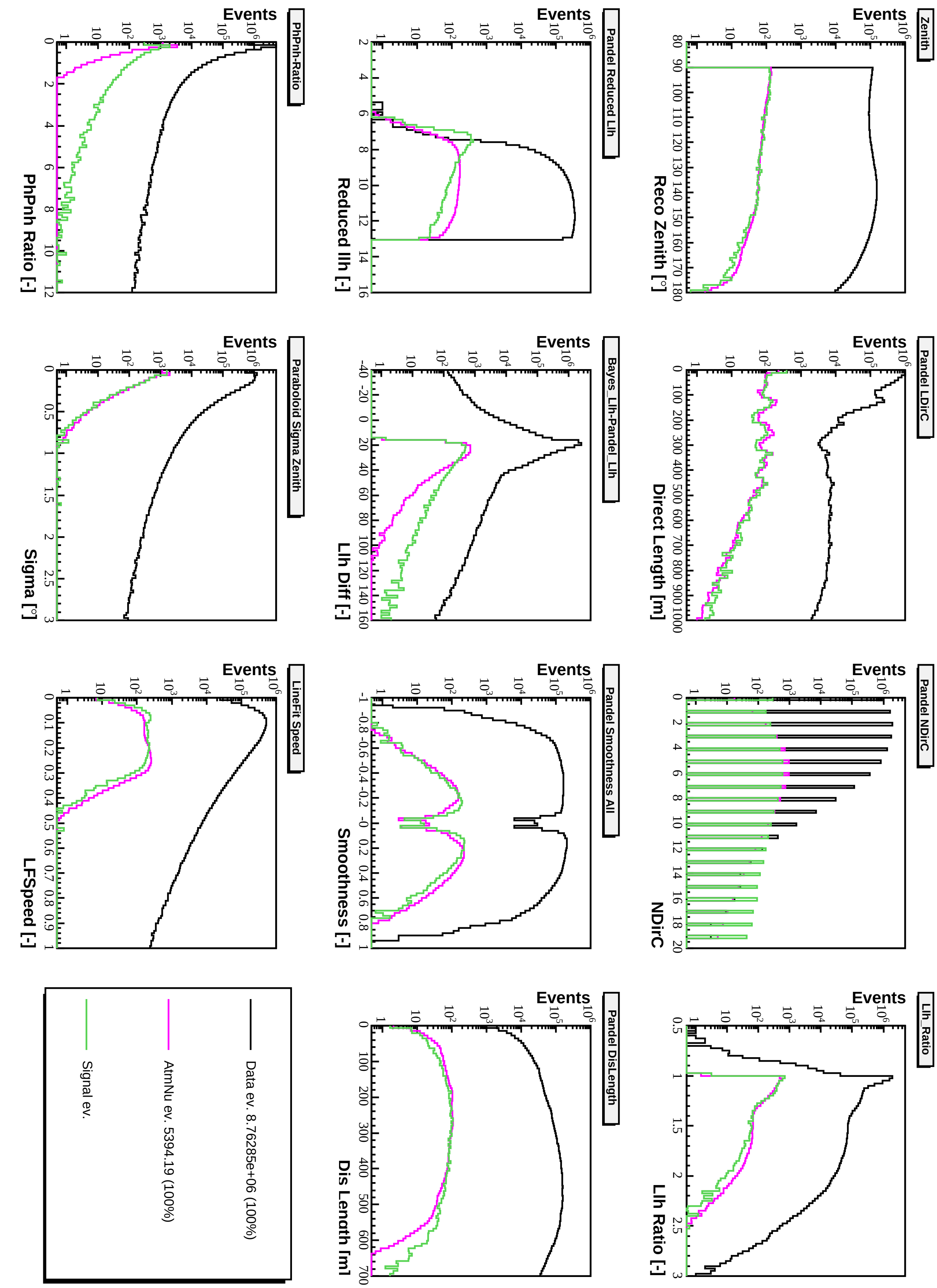

Figure 6.6: Paramter distributions of level 4 processed simulated and experimental data. A zenith angle cut is applied at $\Theta > 90°$. The signal neutrino flux is scaled up for a better illustration. Black: data, green: simulated astrophysical

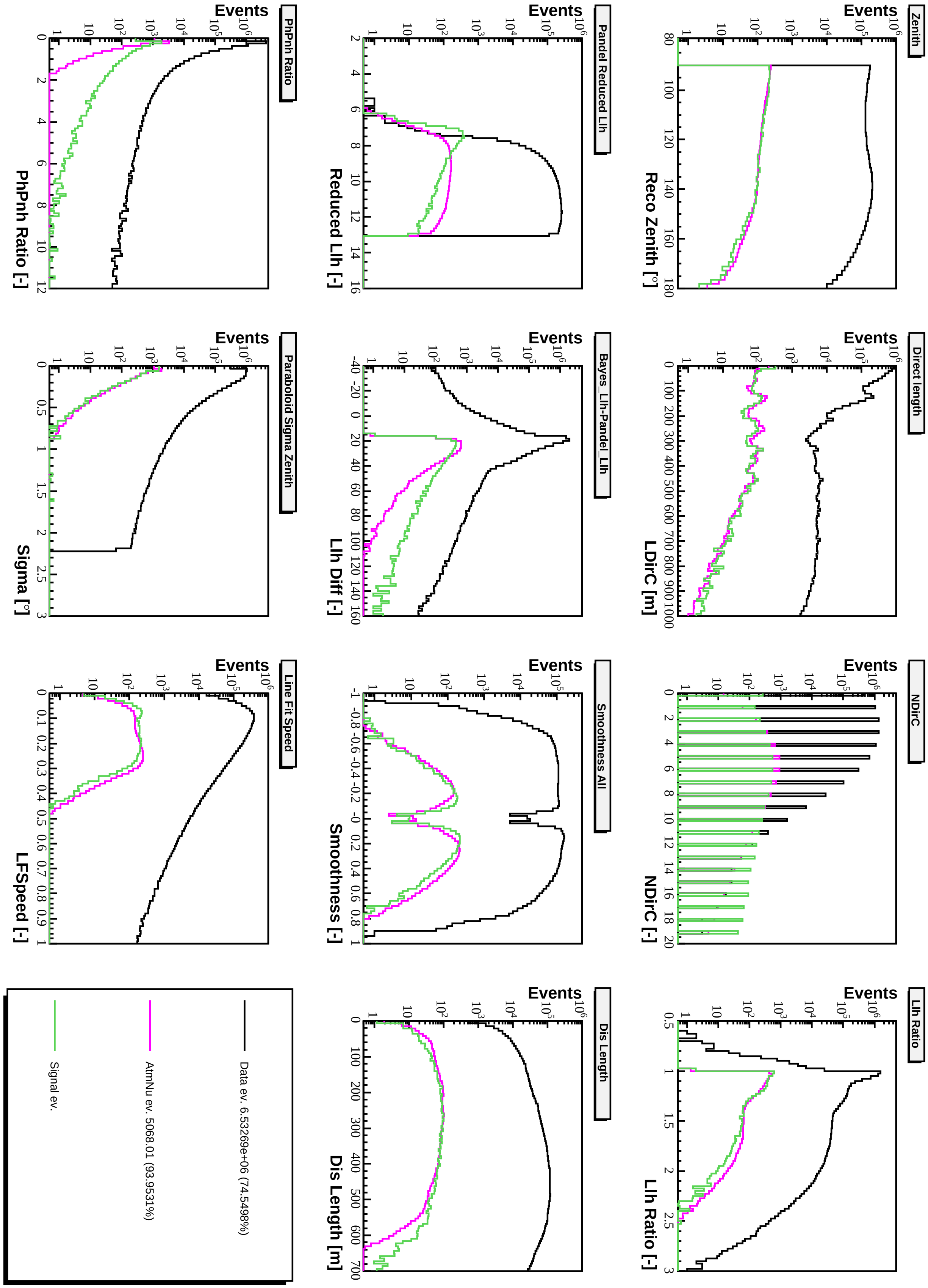

Figure 6.7: The distributions of the parameters after cuts of level 5 have been applied. Black: data, green: simulated astrophysical neutrinos, pink: simulated atmospheric neutrinos.

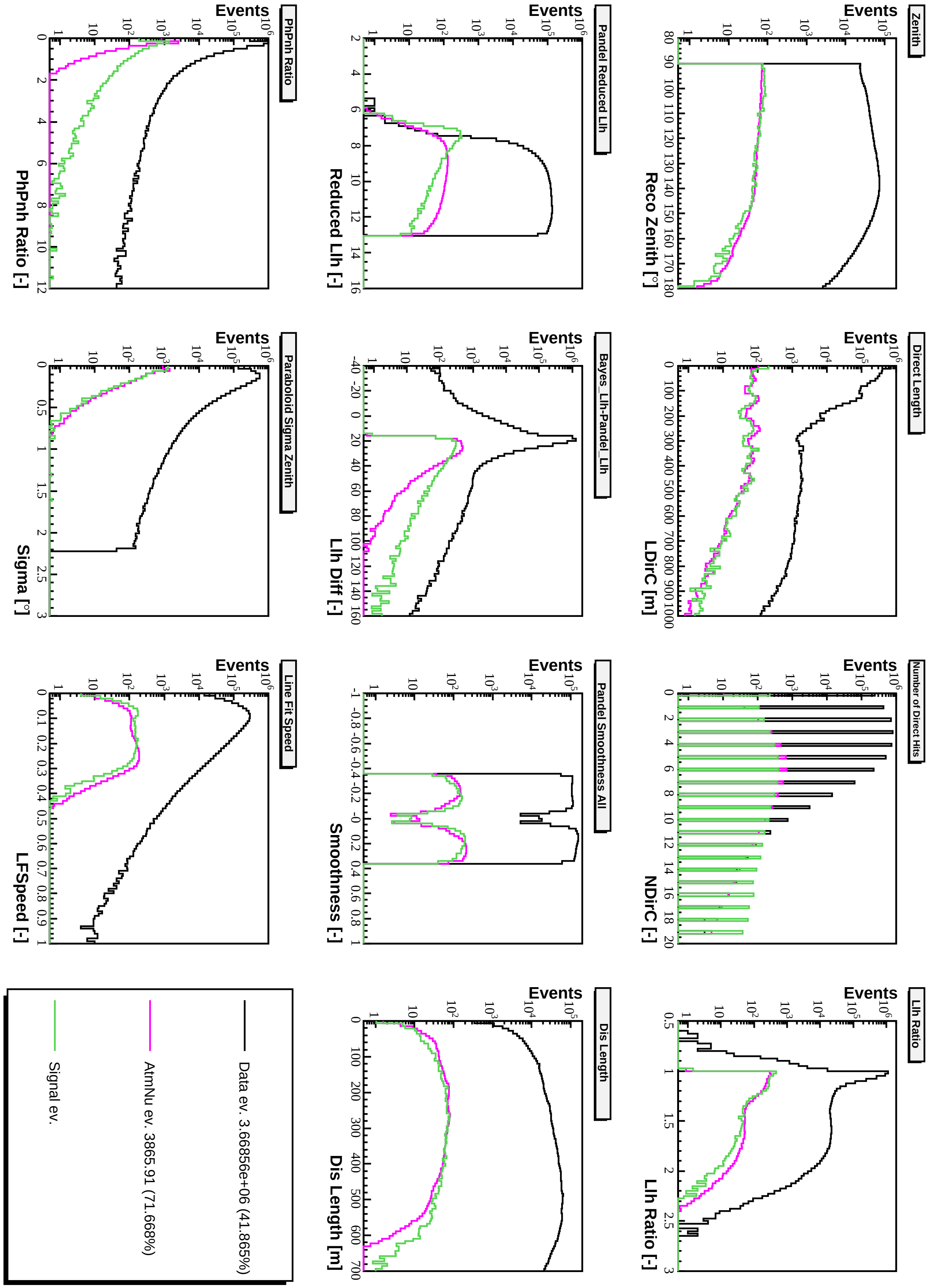

Figure 6.8: The distributions of the parameters after a level 6 cut has been applied. Black: data, green: signal neutrinos, pink: atm. neutrinos

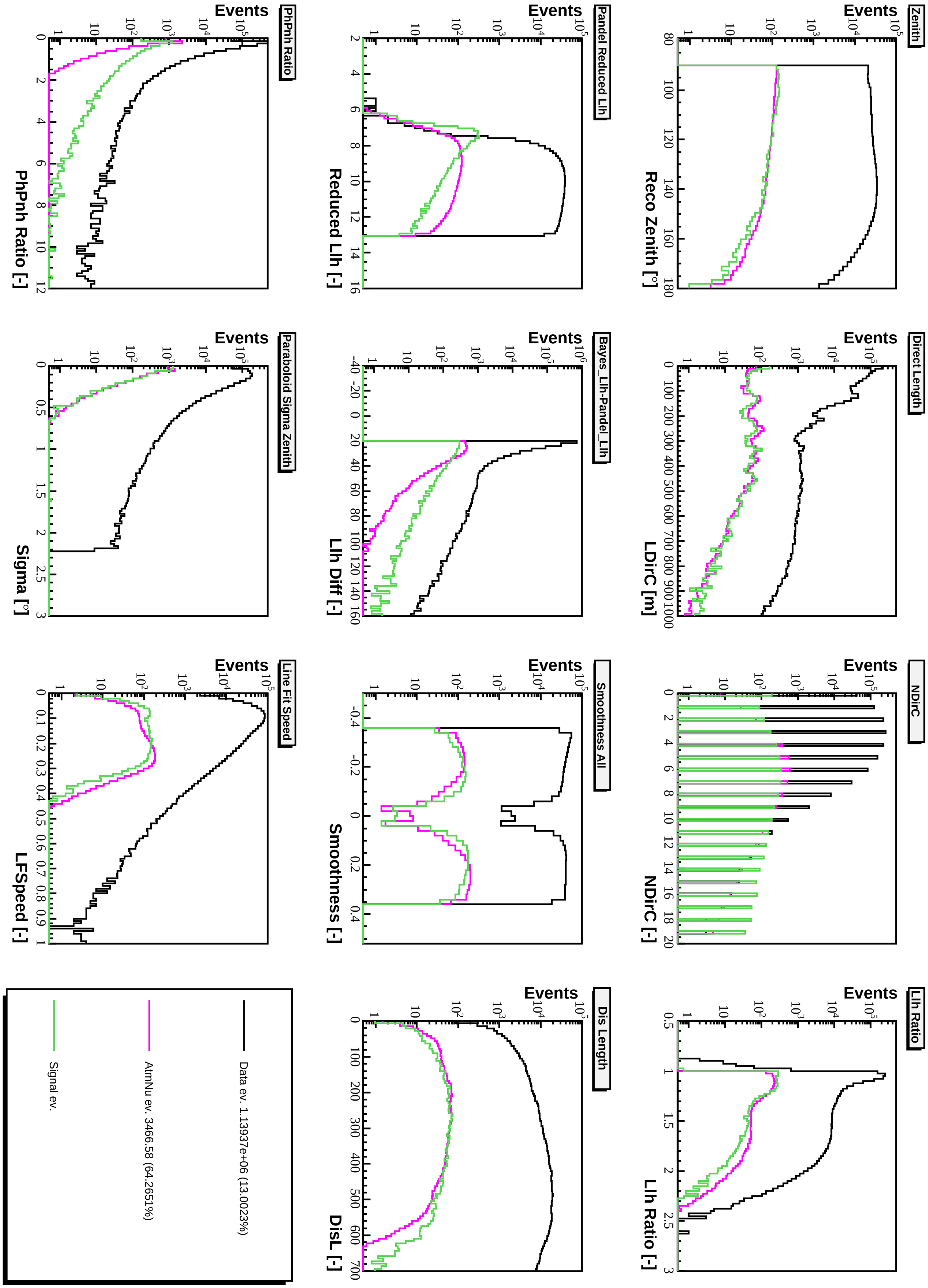

Figure 6.9: The distributions of the parameters after a level7 cut has been applied. Black: data, green: signal neutrinos, pink: atm. neutrinos

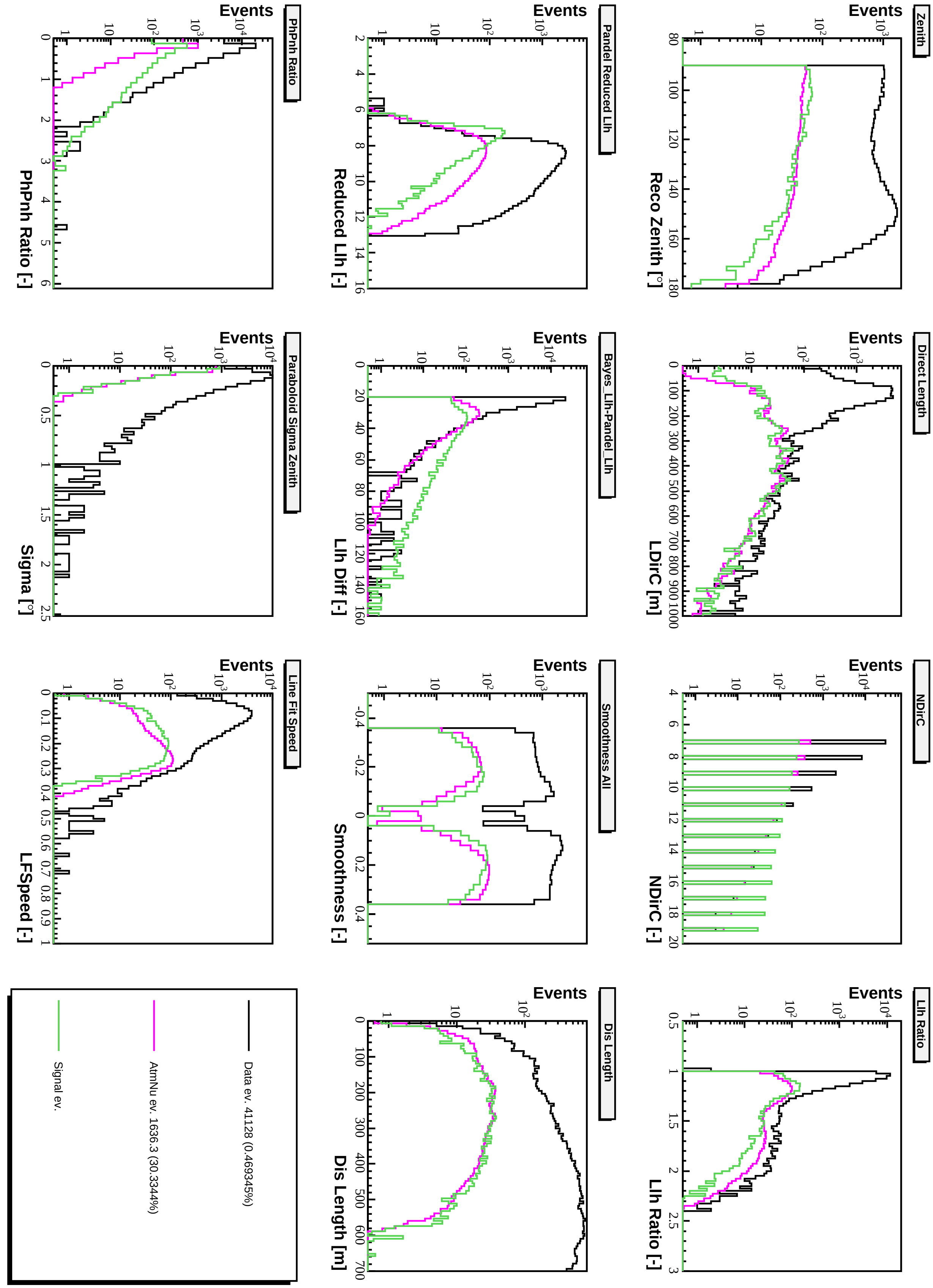

Figure 6.10: The distributions of the parameters after a level8 cut has been applied. Black: data, green: signal neutrinos, pink: atm. neutrinos

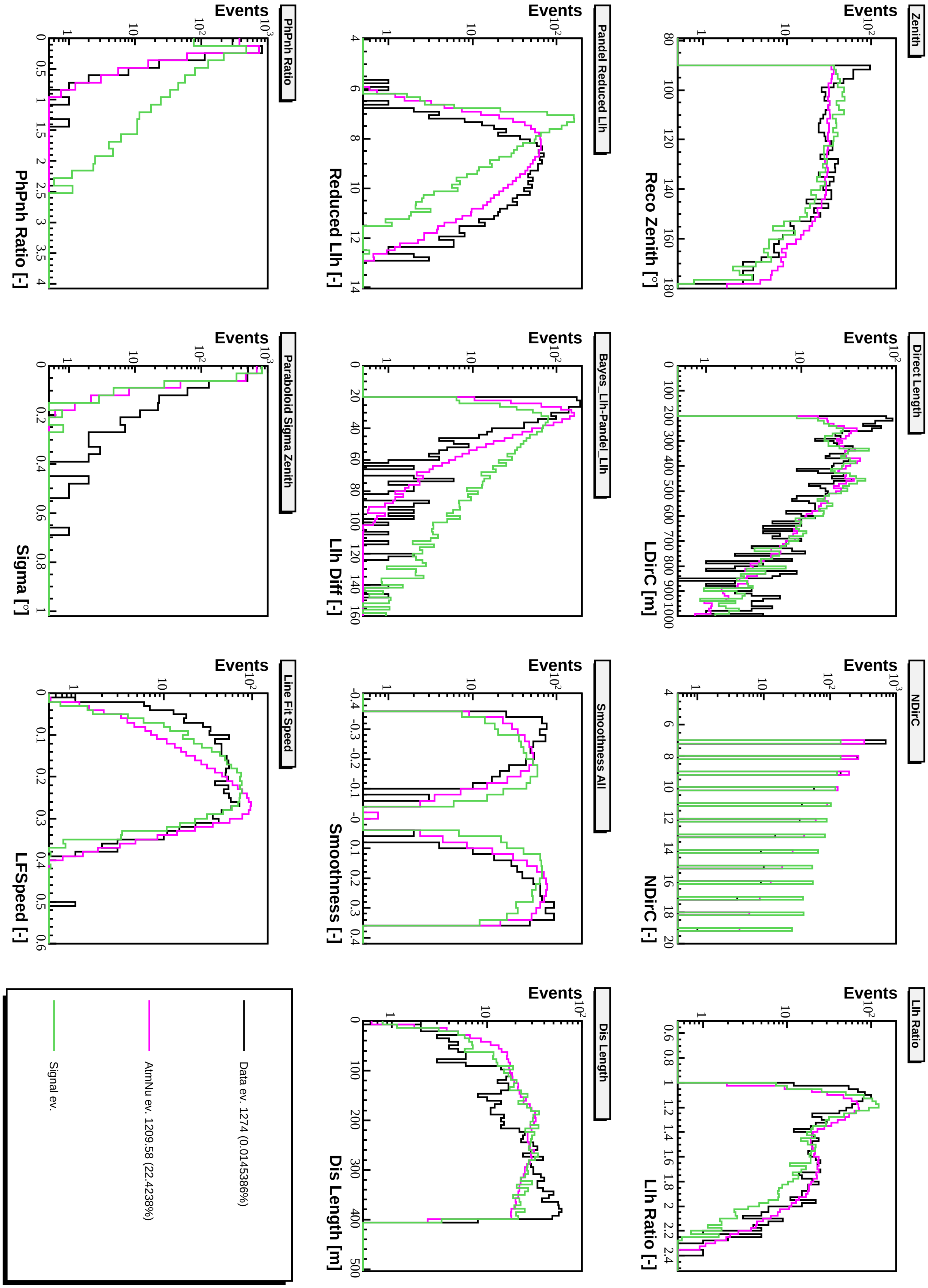

Figure 6.11: Distributions at final cut level. Black: data, green: signal neutrinos, pink: atm. neutrinos

6.3 The Random Forest

The Random Forest method is a classifier based on a collection of decision trees each independently constructed to use a bootstrap sample of a training set. The leaves of the tree finally carry the information about the classification that should be made.

Each event of the sample is characterized by a vector $\mathbf{x}_i$ whose components are the chosen parameters of the detector's output and/or derived quantities. The interference from the N pairs of input and classification (i.e. signal/background) to some kind of output function is called the *training* of the learning method.

Choosing the right input parameters for training is an important task. A parameter variation was performed in order to define an optimized set of parameters with regard to their classification abilities. A technique called *relevance* estimates the importance of each input parameter by the training process and is given by the Gini-Index discussed in the next section. Too many input parameters in relation to the number of training events lead to *overtraining* (see sec.6.3.1). The input is *preprocessed* in the sense that combined parameters x'_i are calculated from the input parameters x_i which are better suited to describe the event. These input parameters form a multidimensional vector space. With successive cuts c on each of the parameter planes the Random Forest extracts a hypercube in this multi-dimensional vector space, whereas the parameters are chosen out randomly.

6.3.1 The Training Process

The most important component of a statistical learning method is its training sample. Monte Carlo simulations are a standard way of generating them. Nevertheless they must be used with care since the simulated events have to match the experimental observations very well. Small features that exist in the simulated data but not in reality may otherwise result in a trained method that handles simulations perfectly, but shows a behavior like random guessing on real data. Futhermore one has to provide enough event statistics for the training process to avoid a phenomenon called *overtraining*.

Overtraining means that too few training samples in a very high dimensional space result in such a low space density that the definition of a complex function by the learning process and its applications to new events will be generally bad.

A basic concept to detect overtraining is the division of the event samples into a training set and a test set which can serve as a reliable check how well the learning method really performs.

For the given purpose of signal from background rejection on an IceCube data sample the training samples contain the two classes neutrinos (usually NuGen Monte Carlo data) and atmospheric muons (usually CORSIKA Monte Carlo).

6.3.2 Decision Trees

The binary tree built up by consecutive tests is called a decision tree. The various decision tree implementations differ in the way how the tree is built, i.e. in what way the pair of input vector and cut value is selected for each node of the tree. The tree growing begins with the complete sample in a single node, the root node, which is identical to the complete parameter space.

In the following, the class separation is achieved by cutting each node into two successor nodes using one randomly chosen parameter once with an optimized cut value to separate the sample. This corresponds with a successive division of the parameter space into hypercubes.

The Random Forest approach defines a *Gini index* [Zim05] as :

$$\text{Gini(D)} = 1 - (p_0(D)^2 + p_1(D)^2). \tag{6.3}$$

Here $p_0(D)$ is the fraction of events from class 0 in the set D and $p_1(D)$ is the fraction of events from class 1 in the same set, whereas the probabilities are approximated by the sampled training events. The Gini Index measures the inequality of two distributions and has a value between zero and one; a low Gini index indicates more equal distributions, whereas a high Gini index shows unequal distributions. The cut is selected in minimizing the sum of the resulting Gini indices. This results in minimizing the variance of the population of signal and background and obviously purifies the sample.

At each node the query by searching through all possible pairs of (x_i,c) is applied until only nodes are left which give a final classification and need no further branching. The final nodesize, i.e the number of remaining events in a final node, may be defined in advance. To each terminal node the remaining event(s) assign(s) a class label l (i.e. 0 for signal 1 for background). For terminal nodes still containing a mixture of events of different classes, a mean value is calculated for l, with $l = N_b/(N_s + N_b)$, taking into account the class populations of signal N_s and background N_b [A+08]. The output for a new event $\mathbf{v}$ is found by descending in the tree structure until a leaf is reached. The leaves of the tree thus contain the final output and they assign a class label l to $\mathbf{v}$, associated with the corresponding slice of input parameter space. The vector $\mathbf{v}$ will be classified by all trees and the average result is calculated as follows:

$$s(v) = \frac{\sum_{i=1}^{n_{trees}} l_i(v)}{n_{trees}} \tag{6.4}$$

[A+08]. This mean classification or *signalness* is used as the only cut parameter in the signal/background separation.

The Random Forest does not make a simplification of the trees by removing branches that are considered irrelelevant which is called *pruning* [A+08]. Instead it creates a set of largely uncorrelated trees and combines their results to make a generalized prediction. The output for each event is thus an average of the outputs of the different classifiers. A method to obtain independent trees is *bootstrapping.* k different training sets of the same size as the original training set are created with replacement from the original one. This solution is especially favorable when dealing with a limited number of training events. The number of the training sets depends on the number of trees that should be grown and can be defined within the program. The number of trees also depends on the convergence of the error σ given by:

$$\sigma(n_{tree}) = \sqrt{\frac{\sum_{i=1}^{n_{sample}} (s_i^{est}(n_{tree}) - s_i^{true})^2}{n_{sample}}}. \tag{6.5}$$

$\sigma(n_{tree})$ is the rms error of the estimated *signalness.* $s_i^{est}(n_{tree})$ denotes the estimated *signalness* (which depends on the number n_{tree} of combined trees) and b_i^{true} is the true *signalness* of event i in the sample, which contains n_{sample} events in total (see [A+08]). Usually 100 trees are sufficient. In the limit of an infinitely large training set each of the k new sets consists of about 63% of the events in the original set, the rest are copies.

6.3.3 The Application of the Random Forest on IceCube Data

For the application of the Random Forest method on the IceCube data the following simulated data sets are used for training. A Corsika generated background sample with a mixture of coincident and single muons normalized to a specified livetime as well as a Monte Carlo set of simulated neutrino events weighted to an atmospheric flux prediction of Honda and Naumov (see chapter 6.2.1). The training was performed with $3 \cdot 10^3$ events of each sample.

A further cut on the reconstructed zenith angle of 85% has been applied to reject the better part of background events.

A number of 10 different reconstruction parameters has been chosen as variables for the training and classification proces. In a first approach different test runs were done in order to determine an optimized combination of parameters with respect to the classification result as well as to check the classification process. The test runs were performed with the same Monte Carlo samples as used for the training process with the first $3 \cdot 10^3$ excluded. Fig. 6.12 shows the output of the classification of the test run.

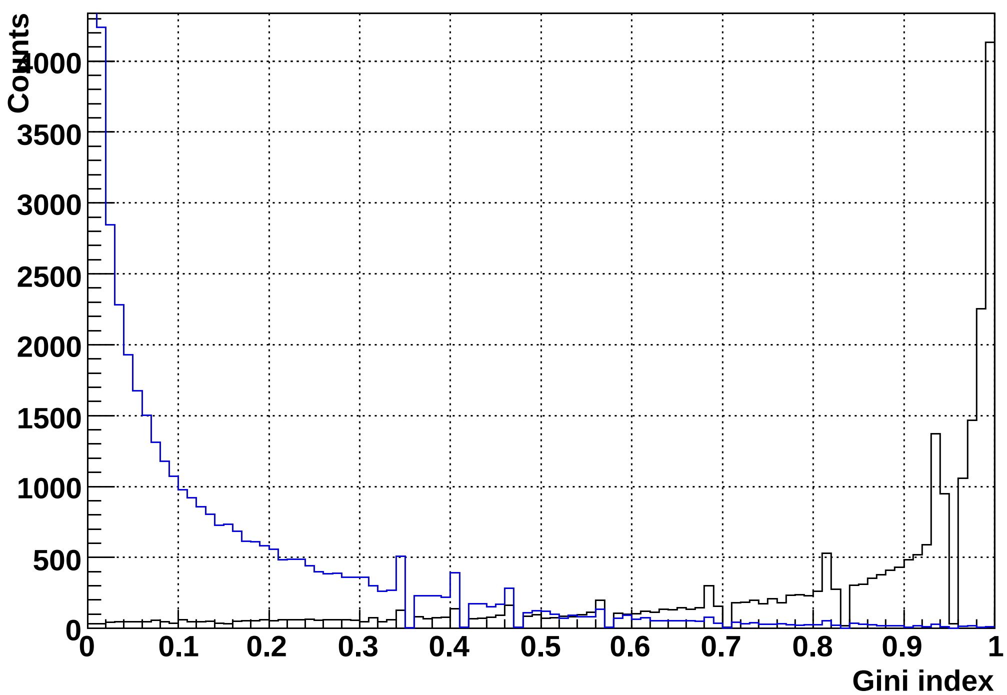

Figure 6.12: The mean classification output of the Random Forest for a tested Monte Carlo sample. The blue line is the atmospheric muon background, the black line shows the simulated neutrino sample.

The events are classified with respect to the calculated *signalness* giving two separate distributions. The classification of the simulated data with the used parameters has obviously worked fine and can further be applied to the experimental data.

Fig. 6.13 and 6.14 show the background rejection factor as well as the signal efficiancy for cuts applied on the *signalness*. A cut of 0.99 provides a signal efficiancy of 67.32% and a background rejection of 99.96%.

With these settings the procedure was executed on the experimental data sample. From the $9.395 \cdot 10^6$ events of the initial dataset 4033 events have survived the cut. This corresponds to 99.96% of the initial data sample and to approximately the number of 67% of the atmospheric neutrino events expected for that livetime, which is 4029.

Fig. 6.15 shows the resulting output of the classification process for the experimental data sample. This sample was further used for the reconstuction of the atmospheric neutrino spectrum which will be discussed in detail in the next section.

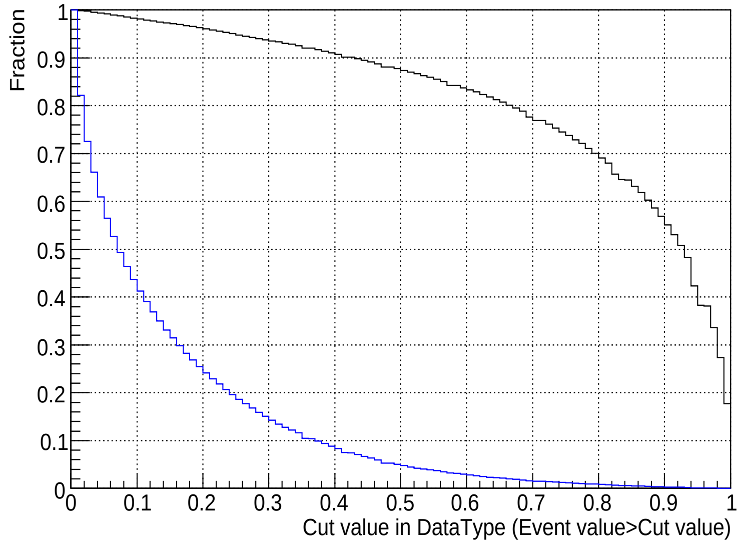

Figure 6.13: The background rejection factor. The plot illustrates the number of events that, for one of both data classes, remain after a cut on the *signalness* has been applied. Black are signal events, while blue denotes background.

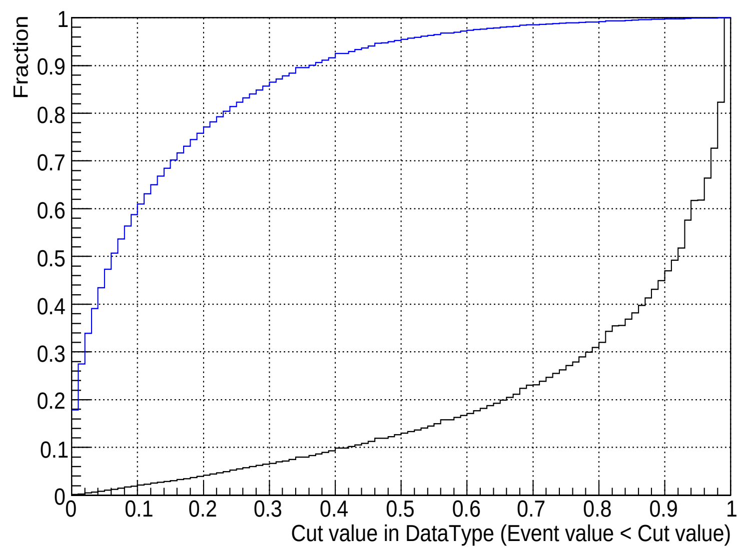

Figure 6.14: The signal efficiency. The plot illustrates the number of events that, for one of both data classes, remains after a cut on the *signalness* has been applied. Black are signal events, while blue denotes background.

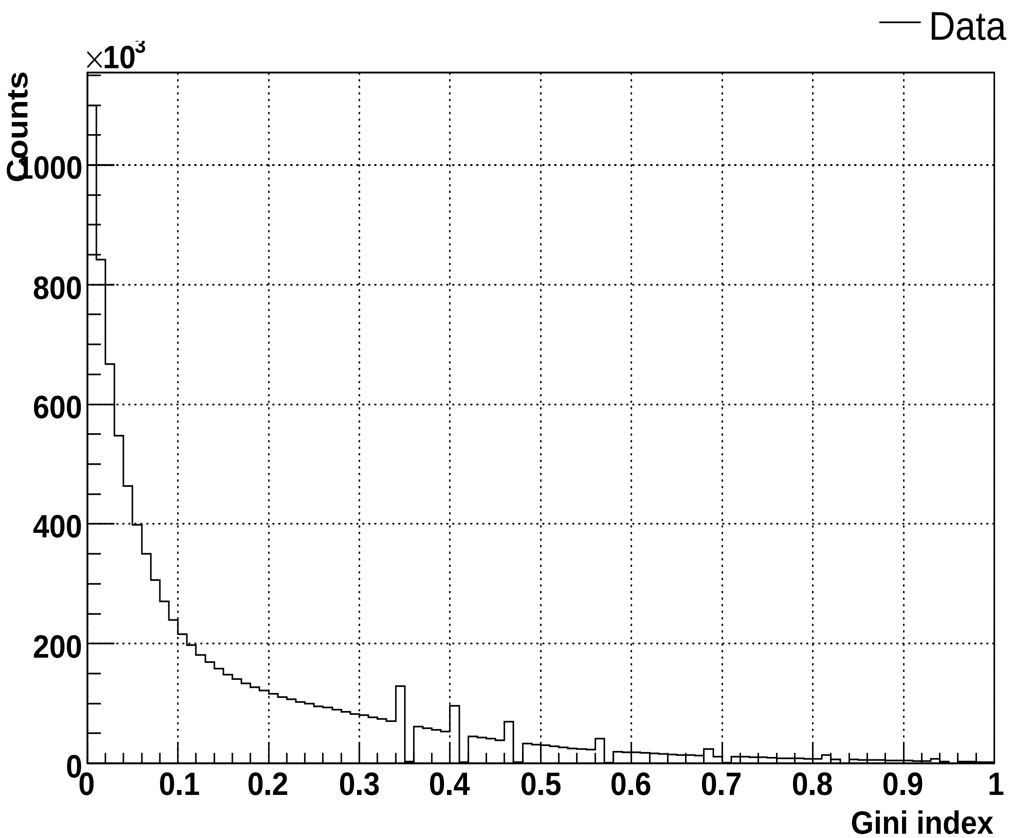

Figure 6.15: The mean classification output for the experimental data sample as a function of the *signalness*. A cut on *signalness* at 0.99 has been applied.

6.4 The Unfolding of the Energy Spectrum

The purpose of this chapter is to describe the theoretical fundamentals for the reconstruction of energy spectra from experimentally measured data. Since the general problem has been stated and the unfolding has been described, different applications are introduced and discussed.

6.4.1 Stating the Problem

A typical task within particle physics experiments is the measuring of the distribution $f(x)$ of a physical quantity x. This might be the distribution of a cross section or as in this thesis an energy distribution. With an ideal detector one could simply measure the quantity x of every event and could obtain $f(x)$ by display of a histogram. With a real detector one has to deal with three effects that distort the measured distributions namely:

- **Limited acceptance** of the detector,
- **Transformation** of the wanted quantity,
- **Finite resolution** of the detector leading to a smearing of the measured quantity.

As a consequence the distribution $g(y)$ of a measured quantity is not identical to the distribution $f(x)$ of the true quantity x. The procedure of correcting these distortions is called **unfolding**. Mathematically the relation between the two distributions can be expressed by the Fredholm integral equation of first kind [Blo02].

$$g(y) = \int A(y,x)f(x)dx + b(y) + \epsilon(y) \tag{6.6}$$

The kernel $A(y,x)$ reflects the detector properties and defines the probability to measure the value y when the true value is x. In practice it is determined by Monte Carlo simulations of the measuring process. On the right hand side there are statistical errors $\epsilon(y)$ and a background distribution $b(y)$ deriving from the meassurement process itself. The background distribution can be independently measured or calculated and is assumed to be known in the following. Finally one gets the relation for the measured distribution $g(y)$. If the number of measured events is sufficiently high the statistical errors can be negelcted. If limited acceptance is the dominant effect of a measurement with high accuracy the above equation can be solved easily. But in case of a high bias of the measured data, because of finite resolution and with no hypothesis of the true distribution, unfolding is the only method to solve the problem. In doing so, one has to handle with a statistically and mathematically ill problem which can have strong oszillating solutions.

6.4.2 Discretization

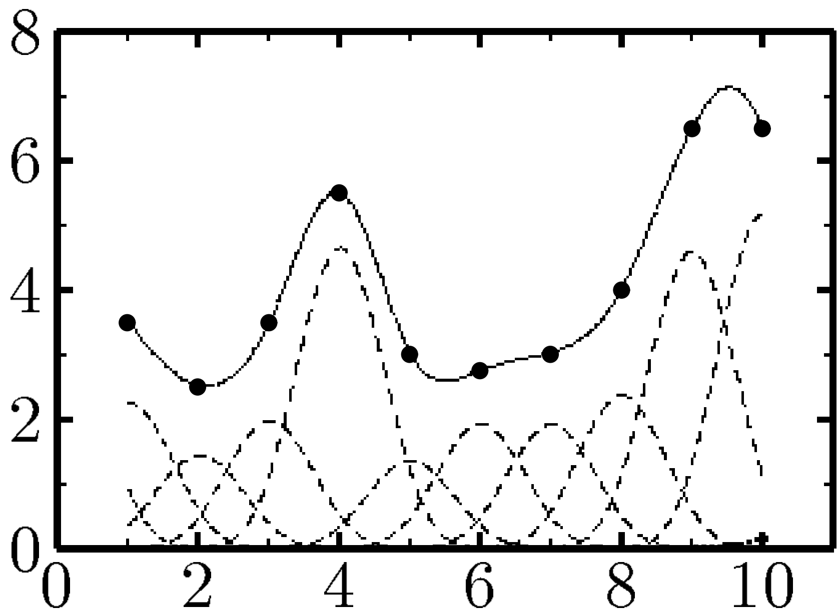

Figure 6.16: Discretization of a function by cubic B-splines. [Lue07]

In the case of discrete varibles x and y the first step in resolving the integral is to replace it by a sum. The functions $f(x)$ and $g(y)$ are then replaced by vectors with elements f_j, $j = 1, 2, \ldots, m$ and g_i, $i = 1, 2, \ldots, n$ and the Fredholm-equation then is:

$$\hat{g}_i = \sum_{j=1}^{m} A_{ij} f_j + b_i + \epsilon_i. \tag{6.7}$$

This step is called the discretization of the integral equation. With a finite number of coefficients $a_1, a_2, \ldots, a_j \ldots a_m$ and basis functions $p_j(x)$ the true distribution $f(x)$ can be parametrizised by a sum as follows:

$$f(x) = \sum_{j=1}^{m} a_j p_j(x), \tag{6.8}$$

where cubic B-splines are chosen as basis functions. Cubic B-splines are polynomials of third order which are positive on an interval between three knots, otherwise zero. The discretization of a function by B-splines is illustrated in Fig. 6.16. In the following all measured distributions are represented by histograms:

$$g_i = \int_{y_{i-1}}^{y_i} g(y)dy, \qquad A_{ij} = \int_{y_{i-1}}^{y_i} A_j(y)dy \tag{6.9}$$

$$b_i = \int_{y_{i-1}}^{y_i} b(y)dy, \qquad \epsilon_i = \int_{y_{i-1}}^{y_i} \epsilon(y)dy, \tag{6.10}$$

with interval boundaries $y_0, y_1, \ldots, y_n$, where n is the number of the histogram bins. With these definitions the matrix element A_{ij} gives the probability to finding the true event of bin f_j of the true distribution in bin g_j of the measured distribution, so that all elements of $A_{ij} \gtrsim 0$. In order to find an estimate for the parameters a_j of (6.8) the method of maximum likelihood is applied. To do so one considers the probability $P\left(\hat{f}_i|f_i\right)$, to find the value $\hat{f}_i$ in bin i when the true value is f_i. As the values f_i depend on the parameter a_j the likelihood function

$$L(a) = \prod_{i=1}^{n} P\left(\hat{f}_i|f_i\right) \tag{6.11}$$

is as well a function of the requestet parameter. The best estimate of a_j is that for which $L(a)$ has a maximum. Instead of maximizing the likelihood function one minimizes the negative logarithm of the likelihood function which is:

$$S(a) = -\sum_{i=1}^{n} \ln P\left(\hat{f}_i|f_i\right). \tag{6.12}$$

6.4.3 Unfolding with Regularization

With a square matrix $\mathbf{A}$ one could solve the equation with standard algebraic methods like matrix inversion as:

$$\hat{\mathbf{f}} = \mathbf{A}^{-1}(\hat{\mathbf{g}} - \mathbf{b}), \tag{6.13}$$

while $\mathbf{A}^{-1}$ is the inverse of $\mathbf{A}$ and $\mathbf{b}$ is assumed to be known.

This approach often leads to fluctuating solutions. Mathematically these fluctuations are caused by insignificantly low components a_j which have large eigenvalues. To avoid them one has to take into account regularization methods, which make an assumption on the smooth distribution of the true solution. For this purpose an additional function is added to the likelihood function, which is a measure of the smoothness of the unfolded function $f(x)$ as:

$$R(a) = S(a) + \frac{1}{2}\tau \cdot r(a), \tag{6.14}$$

where τ is a regularization parameter. The regularization term is given by the total curvature as follows:

$$r(a) = \int \left(\frac{\mathrm{d}^k \mathrm{f}(x)}{\mathrm{d}y^k}\right)^2 \mathrm{dx}. \tag{6.15}$$

The regularized solution a_j^{reg} is connected to the non-regularized solution a_j^{nonreg} via:

$$a_j^{reg} = \frac{1}{1+\tau S_{jj}} a_j^{unreg}, \tag{6.16}$$

where S_{jj} are diagonal elements of the matrix $\mathbf{S}$. The regularization parameter then is determined by the number of degrees of freedom as:

$$n_{df} = \sum_{j=1}^{m} \frac{1}{q+\tau \cdot S_{jj}}. \tag{6.17}$$

This is a very important parameter as it determines the strength of the regularization and has to be chosen thoroughly.

6.4.4 The RUN Program

With the unfolding program RUN by V. Blobel [Blo02] an unfolding can be performed with up to three energy correlated parameters. As input a simulated data file is required, from which the kernel of equation (6.4.1) is computet and which contains the simulated values of the requestet value x in (6.4.1), as well as the file which contains the experimental data to be unfold. A function $f_0(x)$ can be further determined which describes analytically the distribution of the simulated data. As no such function is available, the function is directly determined from the simulated data.

The following parameters of the programm have been used for this analysis:

- **NRDF**: The number of degrees of freedom
- **KNOTS**: The number of knots of the spline function
- **XLIMITS**: Here: Limits on the energy range on which the unfolding was executed

- **XBINS**: The limits of the energy bins
- **VARIABLE**: The number of bins for each of the three variables
- **FXPOSITIVE**: For the function f(x) only positive values admitted
- **SMOOTH**: The function $f_0(x)$ is smoothed

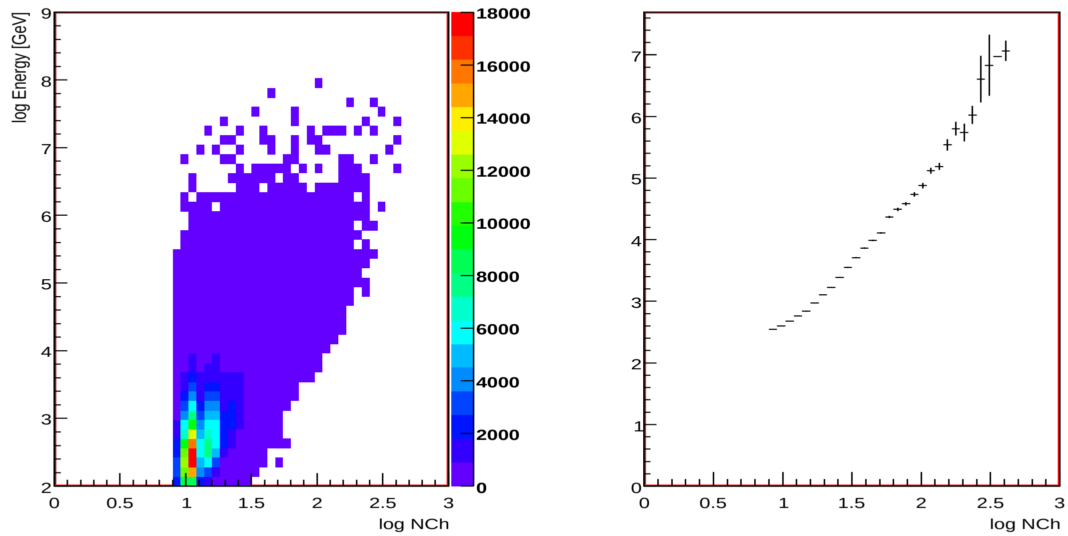

Figure 6.17: Energy correlation of the RUN input variable NChannel.

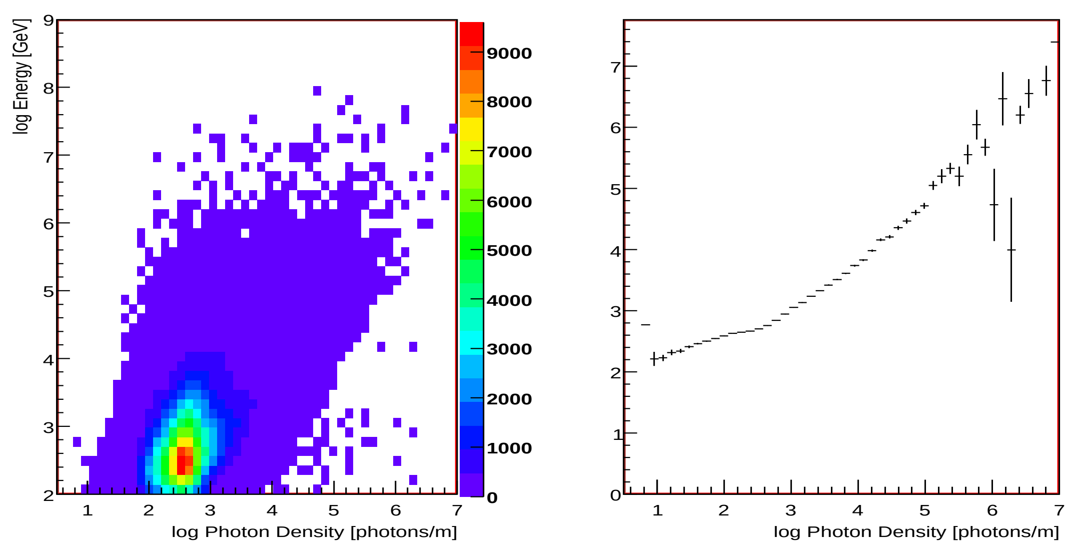

Figure 6.18: Energy correlation of the RUN input variable PDensity.

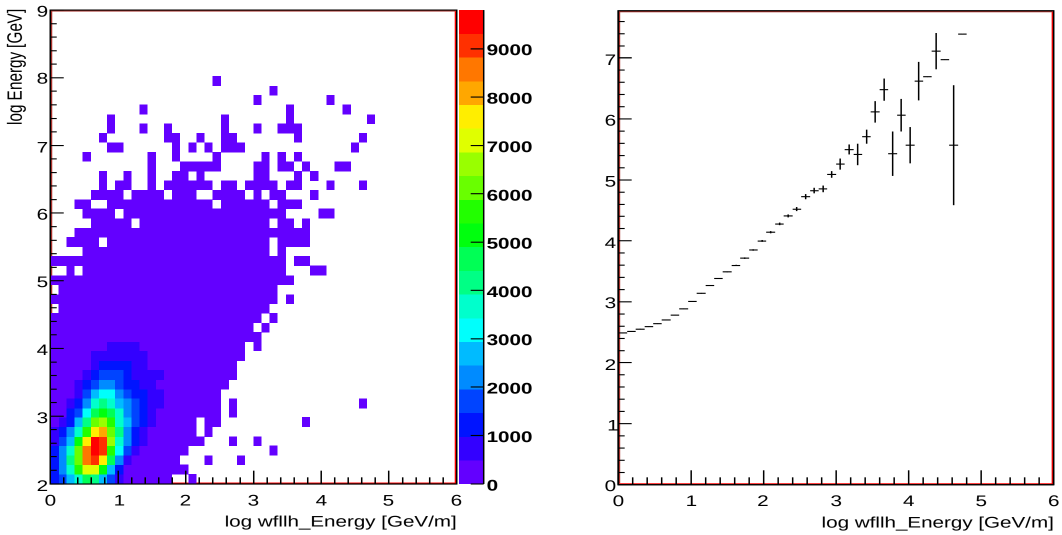

Figure 6.19: Correlation of the RUN input variable wfllg Energy.

6.4.5 Unfolding of the Atmospheric Neutrino Spectrum

As the Random Forest method suggests to deliver the best results, in terms of the signal efficiency, the so obtained dataset is used for the unfolding. With a livetime of 40.42 days the final experimental dataset to be unfolded contains 4033 atmospheric neutrino events. A compound set of simulated atmospheric weighted neutrino Monte Carlo events as well as Monte Carlo signal events, with an assumed spectral index of $\gamma = -2$, are used for the determination of the unfolding kernel.

The suitable parameters for the energy reconstruction are obtained by studying their energy correlation. Figs. 6.17,6.18 and 6.19 show the energy correlation of the parameters finally chosen for the execution:

- **NChannel** (NCh): This is the number of hit DOMs contained in one event. Larger values indicate higher energetic events.
- **Photon Density** (PDensity): The photon density parameter is the result on running "mue", an energy reconstruction algorithm, on the 32-iterative solution of the

parameter	**value**
XLIMITS	2 - 6.5
NRDF	19
KNOTS	25
Binning of the variables	
total charge	29
NCh	18
PDensity	19

likelihood. Its "energy" member is filled with photons per meter track length.

- **total charge**: Total charge of the event given by the integrated charges as part of the "Reco Pulse" (see chapter 5 for details).

In order to find the best combination of the unfolding parameters, which are the number of degrees of freedom and the number of knots of the spline function, a simulated energy spectrum is compared with the unfolded spectrum of the same simulated dataset. The best results have been obtained by the following unfolding parameters:

It is displayed in Fig. 6.20.

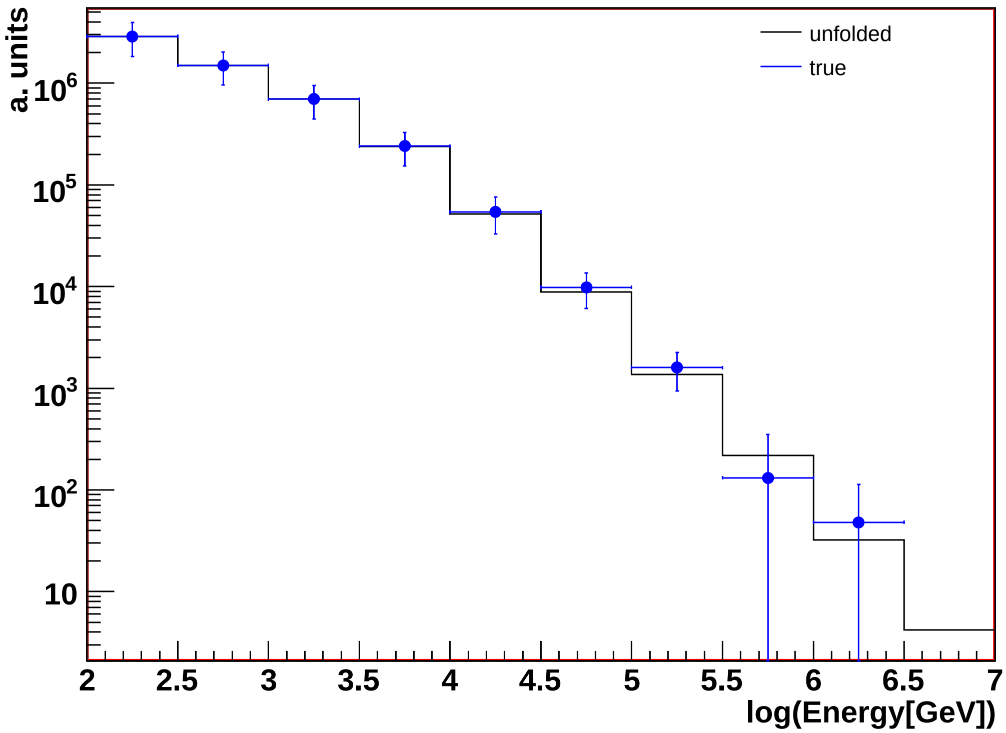

Figure 6.20: Unfolded spectra of simulated atmospheric neutrinos serving as a crosscheck.

Since the unfolding has worked well on simulation the same parameters are used for the unfolding of the experimental data. In Fig. 6.21 the unfolded atmospheric energy spectrum of the selected dataset of the year 2007 (blue dots) is illustrated. For a physical interpretation one has to correct the spectrum on the detector acceptance. As a comparison a pure atmospheric neutrino spectrum was simulated for the analysis (black line) and added to the plot. The error bars contain the unfolding error as well a an assumed systematic error of 30%. The unfolded spectrum agrees well with the simulated spectrum up to an energy range of 10^7 GeV within the error bars. Due to a lack of statistics in the high energy region the error bars are too large to allow a quantitative assessment on measured events.

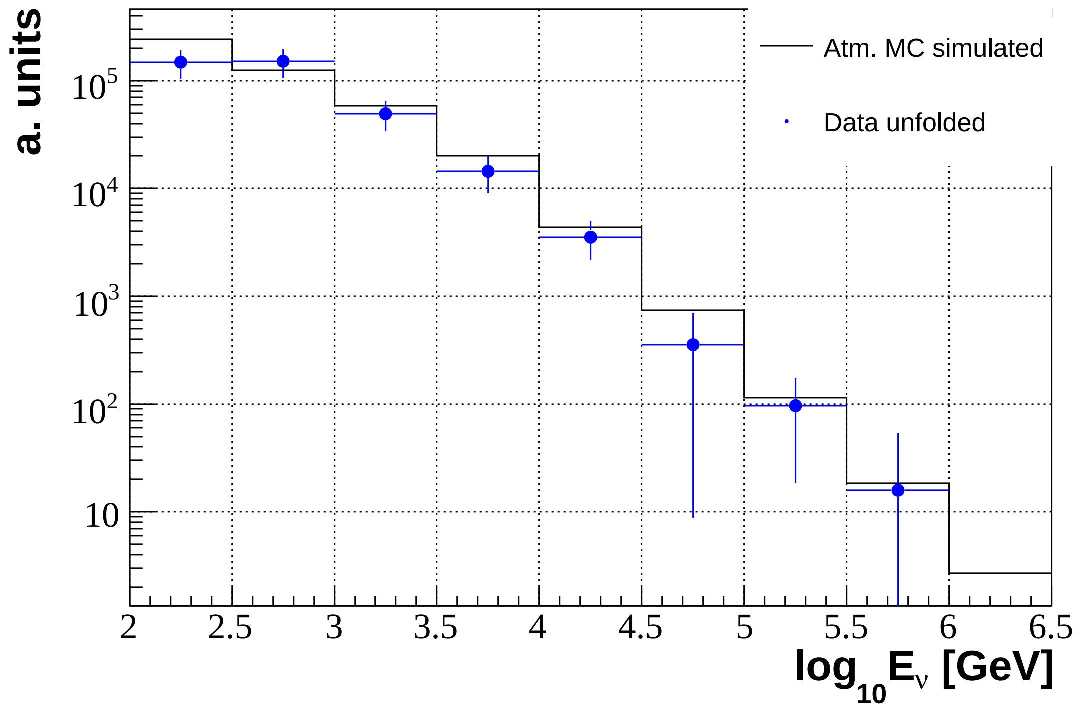

Figure 6.21: Unfolded energy spectrum of the experimental data sample compared to a pure atmospheric energy spectrum displayed in a histogram.

In Figure 6.22 the calculated flux of the unfolded data events is illustrated. The unfolded spectrum, represented by the black dots, is compared with two different atmospheric neutrino flux predictions, by Honda and by Bartol. The upper limit of the shaded areas shows the horizontal flux whereas the lower limit of the areas represents the vertical flux. The unfolded spectrum agrees well with both flux expectations. The errors of the unfolded spectrum are composed of the statistical error and a systematic error. The latter consists mainly of the uncertainty of the atmospheric neutrino flux predictions, which accounts for 25%. Other components of the systematic error are the uncertainties of the neutrino-muon cross section (10%) and the maximum contamination of the data sample by atmospheric muons, which is 5%.

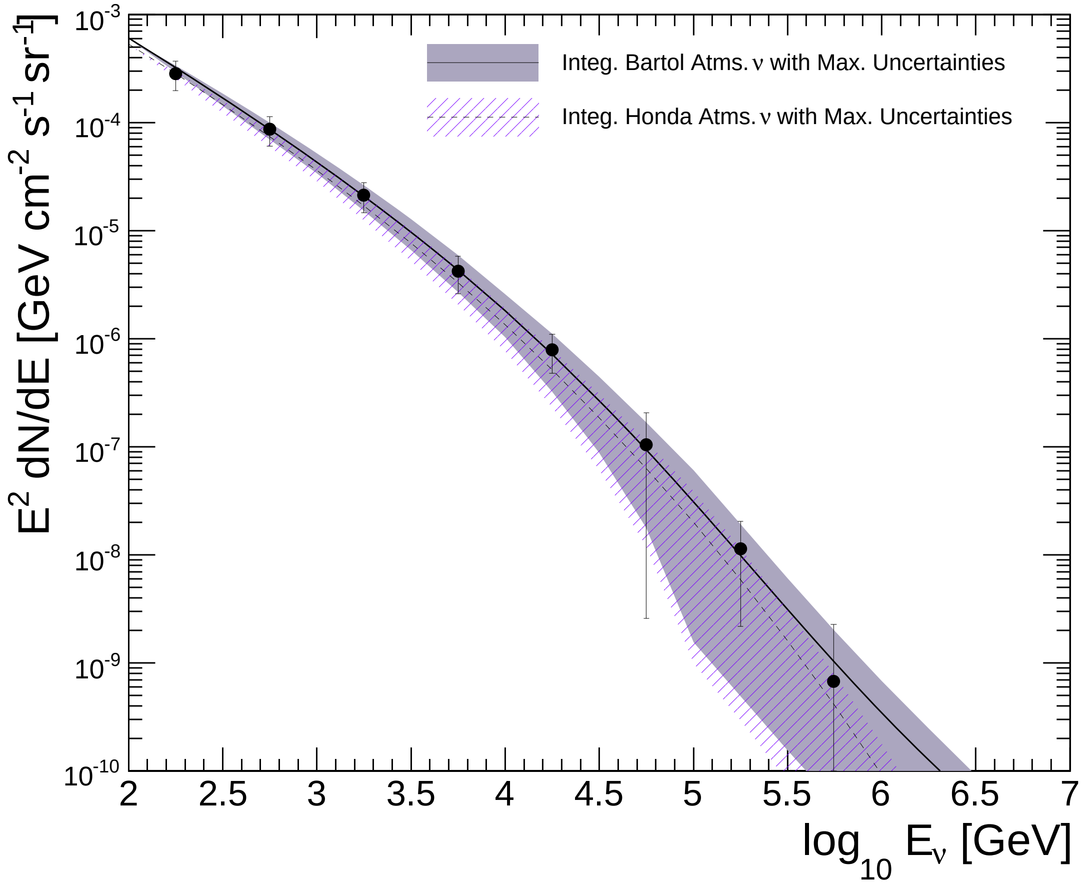

Figure 6.22: The unfolded spectrum weighted with E^2 compared to the predictions of the atmospheric neutrino fluxes by Honda [HKK$^+$06] and Bartol [BGL$^+$04]. The dashed line represents the zenith angle integrated flux predictions by Honda. The continuous line represents the zenith angle integrated flux prediction by Bartol. Black dots are data.

In Figure 6.23 the same unfolded flux is illustrated, but with only the statistical error displayed.

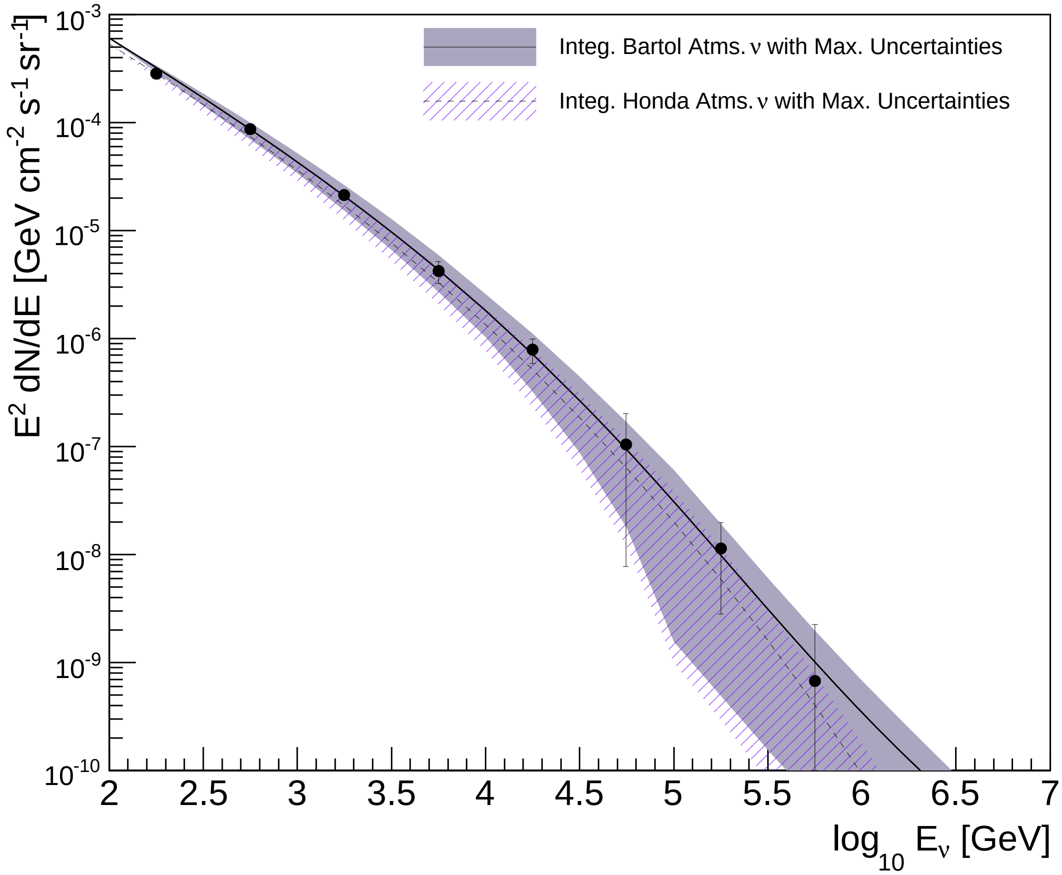

Figure 6.23: The unfolded spectrum weighted with E^2 compared to the predictions of the atmospheric neutrino fluxes by Honda [HKK+06] and Bartol [BGL+04]. The dashed line represents the zenith angle integrated flux predictions by Honda. The continuous line represents the zenith angle integrated flux prediction by Bartol. Black dots are data.

7

Conclusion and Outlook

The task of the IceCube detector is to observe astrophysical neutrino events. The determination of the atmospheric neutrino flux plays a crucial role by achieving this goal as it is the only flux measurable and totally understood so far. The atmospheric flux thus serves as a calibration and verification tool. From an observed excess over the reconstructed atmospheric spectrum, we hope to denote an astrophysical neutrino flux in the energy range above $\sim 10^5\,\mathrm{GeV}$.

AMANDA has measured the atmospheric neutrino spectrum up to $\sim 100\,\mathrm{TeV}$ and IceCube will be able to explore the region, where the prompt neutrino component will dominate. The detection techniques for neutrino observation have to be very mature since the neutrinos can not be detected directly. What serves as a detection device are Čerenkov photons emitted by the secondary particles, the muons, produced when the neutrinos interact with matter in or near the detector volume. Since the distances between the optical modules in the horizontal direction are four times larger than the scattering length of a photon in ice, the observed photons are highly scattered. This additionally complicates the reconstruction process.

The observables measured or parameters derived in IceCube can therefore not be direct parameters of the energy of the incident neutrino but only correlated quantities.

Therefore, in order to reconstruct the energy spectrum of atmospheric neutrinos we have to use unfolding techniques.

For the purpose of this thesis the unfolding method with regularization after Tikhonov has been applied to reconstruct the atmospheric neutrino spectrum from a measured dataset of the IceCube 22-string detector configuration.

To guarantee a good unfolding result the overwhelming atmospheric muon background has to be severely reduced. This type of background can in principle be rejected by restricting the observation to the northern hemisphere. What makes the rejection more complicated are atmospheric muon events which are falsely reconstructed as upgoing, pretending to stem from neutrino interactions.

To successfully reject this type of background events constraints on the quality of the reconstructed track have to be imposed.

For this thesis two different methods have been studied in order to find an optimized background rejection tool. One approach is used by the IceCube point source analyses and for the purpose of this thesis applied for the first time in this extend in order to optimize the signal of atmospheric neutrinos. Namely determining graphical cuts on selected parameter values. Their behavior with respect to the different event classes, namely background and signal, has to be understood very well.

In the thesis at hand a selected set of parameters has been studied intensively by comparing the experimental data with the simulated background and signal. Two classes of background have been assumed, namely single atmospheric muons as well as coincident atmospheric muon events. The latter are likely mis reconstructed because of their special signature in the detector. Simulated data of atmospheric neutrino events weighted with the predictions for the atmospheric neutrino flux by Honda and Naumov has been used. In addition a simulated and weighted astrophysical signal was used as a check.

The results are as follows:

- A signal efficiency for atmospheric neutrinos of 21,6 % was reached with a background rejection of 99.98 %.

Additionally, as a second approach in this thesis, a decision tree algorithm, called Random Forest, was for the first time used in IceCube for the separation of signal and background. As the Random Forest has particular abilities in separating two event classes by applying cuts in a multidimensional parameter space, this method reaches better results.

An optimized set of parameters has been determined corresponding to the classification results of the decision tree. With this method a background rejection of 99.94% can be achieved with a signal efficiency of 61.79%. The cut on the Gini-index was determined with respect to a maximum σ.

In order to achieve a pure data sample this method was further applied on the experimental data. For the unfolding procedure a set of energy correlated variables has been determined which are used as input variables for the unfolding program. In order to determine appropriate unfolding parameters, the unfolding procedure was first applied on simulated data. With the achieved placements the experimental data was finally unfolded. As a result the atmospheric neutrino spectrum could be reconstructed up to an energy of 10^7 GeV.

Because of a low statistic in the energy range above $\approx 3 \cdot 10^5$ GeV the unfolding error is too large to allow a quantitative assessment on measured events.

The aim of future analyses might be to execute this approach on an extended dataset. Since the success of the unfolding method depends to some extend on the energy correlation of the input variables, further results can be improved by developing even better correlated parameters.

Additionally this thesis has shown the potential of the Random Forest method for IceCube analyses. Even more because this method has exposed a high robustness concerning overtraining.

Bibliography

[A$^+$08] Albert u. a.: Implementation of the Random Forest method for the Imaging Atmospheric Cherenkov Telescope MAGIC. In: *Nuclear Instruments and Methods in Physics Research A* 588 (2008), April, S. 424–432. http://dx.doi.org/10.1016/j.nima.2007.11.068. – DOI 10.1016/j.nima.2007.11.068

[Ack06a] Ackermann, M.: *Searches for signals from cosmic point-like sources of high energy neutrinos in 5 years of AMANDA-II data*, Humboldt-Universität Berlin, Diss., 2006

[Ack06b] Ackermann, M. .: Optical properties of deep glacial ice at the South Pole. In: *Journal of Geophysical Research* 111,D13203 (2006), July. http://dx.doi.org/10.1029/2005JD006687. – DOI 10.1029/2005JD006687

[Ans94] Anselmann, P.: GALLEX results from the first 30 solar neutrino runs. In: *Physics Letters B* 327 (1994), Mai, S. 377–385

[BBB$^+$87] Bionta, R. M. ; Blewitt, G. ; Bratton, C. B. ; Caspere, D. ; Ciocio, A.: Observation of a neutrino burst in coincidence with supernova 1987A in the Large Magellanic Cloud. In: *Physical Review Letters* 58 (1987), April, S. 1494–1496

[Bec07] Becker, J.: *NEUTRINOS ON THE ROCKS On the phenomenology of potential astrophysical neutrino sources*, University of Dortmund, Diss., 2007

[BGL$^+$04] Barr, G. D. ; Gaisser, T. K. ; Lipari, P. ; Robbins, S. ; Stanev, T.: Three-dimensional calculation of atmospheric neutrinos. In: *prd* 70 (2004), Juli, Nr. 2, S. 023006–+. http://dx.doi.org/10.1103/PhysRevD.70.023006. – DOI 10.1103/PhysRevD.70.023006

[Blo02] BLOBEL, V.: An Unfolding Method for High Energy Physics Experiments. In: *ArXiv High Energy Physics - Experiment e-prints* (2002), August

[BWC96] BRADLEY W. CARROLL, Dale A. O.: *An Introduction to Modern Astrophysics*. Addison-Wesley, 1996

[Chi04] CHIRKIN, D.: Fluxes of Atmospheric Leptons at 600 GeV - 60 TeV. In: *ArXiv High Energy Physics - Phenomenology e-prints* (2004), Juli

[CR04] CHIRKIN, D. ; RHODE, W.: Propagating leptons through matter with Muon Monte Carlo (MMC). In: *ArXiv High Energy Physics - Phenomenology e-prints* (2004), Juli

[Fes85] FESEFELDT, H.: (1985), Nr. PITHA-85/02

[FNV01] FIORENTINI, G. ; NAUMOV, V. A. ; VILLANTE, F. L.: Atmospheric neutrino flux supported by recent muon experiments. In: *Physics Letters B* 510 (2001), Juni, S. 173–188

[Gai90] GAISSER, Thomas K.: *Cosmic Rays and Particles*. Cambridge University Press, 1990

[GBH08] GRULLON, Sean ; BOERSMA, David J. ; HILL, Gary: *Photonics-based Log-Likelihood Reconstruction in IceCube*. Internal Report icecube/200807001-v3, June 2008

[GHS95] GAISSER, T. K. ; HALZEN, F. ; STANEV, T.: Particle astrophysics with high energy neutrinos. In: *physrep* 258 (1995), Juli, S. 173–236

[Gre66] GREISEN, K.: End to the Cosmic-Ray Spectrum? In: *Physical Review Letters* 16 (1966)

[Gru05] GRUPEN, Claus: *Astroparticle Physics*. Springer-Verlag Berlin, 2005

[HIK+90] HIRATA, K. S. ; INOUE, K. ; KAJITA, T. ; KIFUNE, T. ; KIHARA, K.: Results from one thousand days of real-time, directional solar-neutrino data. In: *Physical Review Letters* 65 (1990), September, S. 1297–1300

[Hil01] HILL, G.: Bayesian event reconstruction and background rejection in neutrino detectors. In: *International Cosmic Ray Conference* Bd. 3, 2001 (International Cosmic Ray Conference), S. 1279–+

[HKK+87] Hirata, K. ; Kajita, T. ; Koshiba, M. ; Nakahata, M. ; Oyama, Y.: Observation of a neutrino burst from the supernova SN1987A. In: *Physical Review Letters* 58 (1987), April, S. 1490–1493

[HKK+06] Honda, M. ; Kajita, T. ; Kasahara, K. ; Midorikawa, S. ; Sanuki, T.: Calculation of atmospheric neutrino flux using the interaction model calibrated with atmospheric muon data. In: *ArXiv Astrophysics e-prints* (2006), November

[HKO08] Halzen, F. ; Kappes, A. ; O'Murchadha, A.: Identifying the Sources of the Galactic Cosmic Rays with IceCube. In: *ArXiv e-prints* 803 (2008), März

[Ice] `http://wiki.icecube.wisc.edu/index.php/TFT_2007_Bandwidth_Analysis`

[Ke91] Kalmykov, N. N. ; et al.: The QGS model predictions and possible variation of hadron interaction at superhigh energies. In: *International Cosmic Ray Conference* Bd. 4, 1991 (International Cosmic Ray Conference), S. 217–+

[Kf08] Klein, S. R. ; for the IceCube Collaboration: IceCube: A Cubic Kilometer Radiation Detector. In: *ArXiv e-prints* 807 (2008), Juni

[LM00] Learned, J. G. ; Mannheim, K.: High-energy neutrino astrophysics. In: *Annu. Rev. Nucl. Part. Sci.* 50 (2000), S. 679

[LMW+07] Lundberg, J. ; Miočinović, P. ; Woschnagg, K. ; Burgess, T. ; Adams, J. ; Hundertmark, S. ; Desiati, P. ; Niessen, P.: Light tracking through ice and water. Scattering and absorption in heterogeneous media with PHOTONICS. In: *Nuclear Instruments and Methods in Physics Research A* 581 (2007), November, S. 619–631. `http://dx.doi.org/10.1016/j.nima.2007.07.143`. – DOI 10.1016/j.nima.2007.07.143

[Lue07] Luenemann, J.: *Entfaltung des Energiespektrums atmosphärischer Myonen mit dem AMANDA-Neutrinoteleskop*, Universität Dortmund, Diplomarbeit, Mai 2007

[Mio01] Miočinović, P.: *Muon energy reconstruction in the Antarctic Muon And Neutrino Detector Array (AMANDA)*, University of California at Berkeley, Diss., 2001

[MPR01] Mannheim, K. ; Protheroe, R. J. ; Rachen, J. P.: Cosmic ray bound for models of extragalactic neutrino production. In: *Physical Review D* 63 (2001), S. 23003

[Mue07] Muenich, Kirsten: *Messung des atmosphärischen Neutrinospektrums mit dem AMANDA-II Detektor*, Fachbereich Physik, Universität Dortmund, Diss., November 2007

[Pan96] Pandel, D.: *Bestimmung von Wasser- und Detektorparametern und Rekonstruktion von Myonen bis 100 TeV mit dem Baikal-Neutrinoteleskop NT-72*, Humboldt-Universität zu Berlin, Diplomarbeit, February 1996

[Pre06] Pretz, J.: *Detection of Atmoshperic Muon Neutrinos with the IceCube 9-string Detector*, University of Maryland, Diss., 2006

[Pro98] Protheroe, R. J.: Origin and Propagation of the Highest Energy Cosmic Rays. In: Shapiro, M. M. (Hrsg.) ; Silberberg, R. (Hrsg.) ; Wefel, J. P. (Hrsg.): *Towards the Millennium in Astrophysics, Problems and Prospects. International School of Cosmic Ray Astrophysics 10th Course*, 1998, S. 3–+

[Rf08] Roulet, E. ; for the Pierre Auger Collaboration: Recent results from the Pierre Auger Observatory. In: *ArXiv e-prints* (2008), September

[Rou00] Roulet, E.: Neutrino Astrophysics. In: *ArXiv Astrophysics e-prints* (2000)

[Som05] Sommers, P.: In: *29th International Cosmic Ray Conference*, 2005

[SS96] Stecker, F. W. ; Salamon, M. H.: High Energy Neutrinos from Quasars. In: *Space Science Reviews* 75 (1996), S. 341

[Sta04] Stanev, Todor: *High Energy Cosmic Rays*. Praxis Publishing Ltd, Chichester, UK, 2004

[The04] The AMANDA Collaboration: J. Ahrens: Muon Track Reconstruction and Data Selection Techniques in AMANDA. In: *ArXiv Astrophysics e-prints* (2004), Juli

[The05] The IceCube Collaboration: The IceCube Collaboration: contributions to the 29th International Cosmic Ray Conference (ICRC 2005), Pune, India, Aug. 2005. In: *ArXiv Astrophysics e-prints* (2005), September

[TIG96] Thunman, M. ; Ingelman, G. ; Gondolo, P.: Charm production and high energy atmospheric muon and neutrino fluxes. In: *Astroparticle Physics* 5 (1996), Oktober, S. 309–332

[Vol80] Volkova, L. V.: Energy Spectra and Angular Distributions of Atmospheric Neutrinos. In: *Soviet Journal of Nuclear Physics* 31 (1980), S. 784–+

[Wag04] Wagner, Wolfgang: *Design and Realisation of a new AMANDA Data Acquisition System with Transient Waveform Recorders*, Fakultät für Physik, Universität Dortmund, Diss., Oktober 2004

[Wax00] Waxman, E.: High Energy Cosmic-Rays and Neutrinos from Cosmological Gamma-Ray Burst Fireballs. In: *Physica Scripta Volume T* 85 (2000), S. 117–+

[WBB+03] Wentz, J. ; Brancus, I. M. ; Bercuci, A. ; Heck, D. ; Oehlschläger, J. ; Rebel, H. ; Vulpescu, B.: Simulation of atmospheric muon and neutrino fluxes with CORSIKA. In: *prd* 67 (2003), April, Nr. 7, S. 073020–+

[Wie] Wiebusch, C.: *Muon Energy Reconstruction with AMANDA*. – DESY IfH

[YT93] Yoshida, S. ; Teshima, M.: Energy Spectrum of Ultra-High Energy Cosmic Rays with Extra-Galactic Origin. In: *Progress of Theoretical Physics* 89 (1993), S. 833

[ZB02] Zier, C. ; Biermann, P. L.: Binary black holes and tori in AGN. II. Can stellar winds constitute a dusty torus? In: *Astronomy & Astrophysics* 396 (2002), S. 91

[Zim05] Zimmermann, Jens: *Statistical Learning in High Energy and Astrophysics*, Fakultät für Physik, Ludwig-Maximilians-Universität München, Diss., June 2005

[ZK66] Zatsepin, Georgi T. ; Kuzmin, Vadim A.: Upper Limit Of The Spectrum Of Cosmic Rays. In: *Pisma Zhurnal Eksp. Teor. Fiziki* 4 (1966), S. 114

Appendix A

Affidavit

I hereby declare that this diploma thesis has been written only by the undersigned and without any assistance from third parties.

Furthermore, I confirm that no sources have been used in the preparation of this thesis other than those indicated in the thesis itself.

Dortmund, 2008-10-13